KU LEUVEN

FACULTEIT WETENSCHAPPEN

Probing flickering variability in cataclysmic variable stars

Marie VAN DE SANDE

Promotor: Dr. Simone Scaringi
KU Leuven

Co-promotor: Prof. Dr. Christian Knigge
University of Southampton

Proefschrift ingediend tot het
behalen van de graad van
Master of Science in de Sterrenkunde

Academiejaar 2013-2014

Contents

Preface

Cataclysmic variables are binary systems consisting of a low-mass red dwarf and an accreting white dwarf. Mass is transferred from the red dwarf to the white dwarf in these systems, resulting in the formation of an accretion disc around the white dwarf. Aperiodic broadband flickering variability is generated by the accretion disc. Flickering variability has previously been studied in great detail in X-ray binaries (XRBs) and Active Galactic Nuclei (AGN). In these systems, the accreting object is respectively a neutron star or a black hole. Because these accreting systems all show flickering variability and other accretion-induced variabilities, it is thought that the physics governing the accretion induced variability is independent of the accreting object.

One of the properties of flickering variability is the linear rms-flux relation, which relates the rms amplitude of the variability of a light curve to its mean flux. The rms-flux relation has been detected in several XRBs and AGN, and so far in only one CV. With the advent of the NASA *Kepler* mission, large amounts of data suitable for its detection in CVs are now available. The aim of this thesis is to detect the rms-flux relation in as many CVs as possible in the *Kepler* field-of-view and to enforce the hypothesis of the universal nature of accretion.

I would like to thank my promotor Simone Scaringi and co-promotor Christian Knigge. The more I worked on this thesis, the more interesting the subject became. This is in great part due to their supervision and extensive knowledge on the subject. Part of this thesis is made during an Erasmus exchange to the University of Southampton. The Erasmus coordinators of KU Leuven and the University of Southampton have helped me a lot during the application process, for which I am thankful. I would like to thank the staff of the Institute for Astronomy of KU Leuven and the School of Physics and Astronomy of the University of Southampton for the pleasant atmosphere, in which the long days of work did not seem as long. And last but not least, I would like to thank my family and friends, who have supported me not only during the making of this thesis but throughout my entire studies.

This research has made use of the SIMBAD database, operated at CDS, Strasbourg, France. This paper includes data collected by the *Kepler* mission. Funding for the *Kepler* mission is provided by the NASA Science Mission directorate. All of the data presented in this paper were obtained from the Mikulski Archive for Space Telescopes (MAST). STScI is operated by the Association of Universities for Research in Astronomy, Inc., under NASA contract NAS5-26555. Support for MAST for non-HST data is provided by the NASA Office of Space Science via grant NNX13AC07G and by other grants and contracts.

Summary

The physics governing accretion discs surrounding compact objects is thought to be independent of the mass, size or type of the central compact object: the nature of accretion is thought to be universal. This hypothesis is built on the common characteristics that all accreting compact objects share, such as similar aperiodic broad-band variability, also referred to as flickering. One of the fundamental properties of this flickering is the rms-flux relation, which is a linear relation between the rms amplitude of the variability of a light curve and its mean flux. The presence of the rms-flux relation in accreting compact objects can be used to rule out some accretion disc models, as it implies that short and long time scale flickering are coupled together multiplicatively. The rms-flux relation has previously been detected in the X-ray light curves of active galactic nuclei and X-ray binaries. By using *Kepler* data, it was recently shown that the cataclysmic variable (CV, accreting white dwarf) MV Lyrae also displays this relation at optical wavelengths. In this thesis, we search for the rms-flux relation within all CVs in the *Kepler* field. We find that the rms-flux relation is consistently found in systems where the data quality allows its detection. This result strongly enforces the hypothesis of the universal nature of accretion onto compact objects.

Er wordt gedacht dat de natuurwetten die accretieschijven omheen compacte objecten beschrijven onafhankelijk zijn van de massa, grootte en type van het centrale compacte object, of met andere woorden, dat de aard van massaoverdracht universeel is. Deze hypothese is gebaseerd op de gemeenschappelijke eigenschappen die alle compacte systemen met massaoverdracht delen, zoals aperiodische breedband variabiliteit, ook "flickering" genoemd. Eén van de fundamentele eigenschappen van flickering is de rms-flux relatie bij accreterende compacte objecten. Dit is een lineaire relatie tussen de rms amplitude van de variabiliteit van een lichtcurve en haar gemiddelde flux: hoe meer variabiliteit, hoe helderder. De aanwezigheid van de rms-flux relatie kan gebruikt worden om enkele accretieschijfmodellen uit te sluiten, aangezien dit impliceert dat de flickering op korte en lange tijdsschaal dienen vermengivuldigd te worden. De rms-flux relatie is reeds ontdekt in de lichtcurves in het X-stralen domein van "active galactic nuclei" en "X-ray binaries". Door middel van *Kepler* data is er recent ontdekt geweest dat de cataclysmische variabele (CV, accreterende witte dwerg) MV Lyrae ook de rms-flux relatie vertoont in het optisch domein. In deze thesis zoeken we naar de rms-flux relatie in alle CVs waarvoor *Kepler* data beschikbaar is. We vinden dat de rms-flux relatie steeds gevonden wordt in systemen waarvan de kwaliteit van de data haar detectie toelaat. Dit resultaat versterkt de hypothese van de universele aard van massaoverdracht.

Vulgariserende samenvatting

Cataclysmische variabelen (CVs) zijn dubbelsterren die bestaan uit een doorsnee ster en een witte dwerg (het massieve eindstadium in de evolutie van de meeste sterren). De meeste dubbelsterren bestaan uit twee sterren, maar bij CVs is er nog een derde component: een accretieschijf. Deze schijf ontstaat omdat de doorsnee ster massa overdraagt aan de witte dwerg. De materie valt echter niet rechtstreeks op de witte dwerg in, maar cirkelt er omheen en vormt zo een schijf omheen de witte dwerg. Binnen deze accretieschijf beweegt de materie zich in zo goed als cirkelvormige bewegingen naar het oppervlak van de witte dwerg toe.

De accretieschijf is de oorzaak van de tot de verbeelding sprekende naam "cataclysmische variabelen". Geregeld vindt er een plotse uitbarsting van energie plaats. Tijdens zulke uitbarsting neemt de helderheid van de CV zo hard toe dat ze oorspronkelijk novae, oftewel nieuwe sterren, werden genoemd. In deze thesis zijn we echter geïnteresseerd in de perioden tussen uitbarstingen in, de inactieve perioden. Tijdens inactieve perioden kunnen we de variabiliteit die door de accretieschijf wordt uitgezonden bestuderen. Deze variabiliteit wordt ook "flickering" genoemd. Dit soort variabiliteit wordt niet alleen gevonden in CVs, maar ook in andere dubbelsterren met een accretieschijf, zoals "X-ray binaries" (XRBs) en "Active Galactic Nuclei" (AGN), waarin de accretieschijf respectievelijk omheen een neutronenster en een zwart gat is. Naast flickering delen deze drie verschillende systemen nog andere eigenschappen. Deze eigenschappen hebben allemaal te maken met de massaoverdracht en de accretieschijf in deze systemen. Dit leidt tot de hypothese dat de natuurwetten die de massaoverdracht beschrijven onafhankelijk zijn van het object waar de massa op invalt, de hypothese van de universele aard van massaoverdacht.

Eén van de eigenschappen van flickering is de rms-flux relatie. Dit is een lineaire relatie tussen de variabiliteit van een lichtcurve en haar gemiddelde helderheid: hoe meer variabel, hoe helderder. De rms-flux relatie is meerdere malen gevonden in XRBs en AGN. Met behulp van de grote hoeveelheden data van NASA's *Kepler* satelliet, is het nu mogelijk om flickering ook in CVs te bestuderen. Desondanks is de rms-flux relatie nog maar één keer ontdekt in een CV.

In deze thesis worden acht CVs waarvoor *Kepler* data beschikbaar is bestudeerd. De rms-flux relatie wordt teruggevonden in twee van hen. Voor de overige CVs laat de kwaliteit van de data ons niet toe om de relatie te ontdekken. Onze bevindingen brengen het totale aantal CVs met een ontdekte rms-flux relatie van één naar drie. Bovendien bevestigen ze de hypothese van de universele aard van massaoverdracht.

List of Figures

List of Tables

Chapter 1

Introduction

1.1 Cataclysmic variables

Cataclysmic variables (CVs) are binary systems consisting of a white dwarf and a low-mass red dwarf. Following conventions, the more massive white dwarf is also called the *primary* and the low-mass red dwarf the *secondary* of the system. Unlike most binary systems, these two stars are not the only components of CVs: the white dwarf is surrounded by an *accretion disc*, created by mass transferred from the secondary to the white dwarf. It is the accretion disc that gives rise to their captivating name and to the wide range of astrophysical phenomena that CVs display on a wide range of time scales [19, 55].

Thermonuclear runaways of matter piling up on the white dwarf (*classical nova eruptions*) and large releases of gravitational energy within the disc (*dwarf nova outbursts*) are the namesake of CVs. These events are violent and sudden: they increase the brightness of the system dramatically for a period of time ranging from several hours to a couple of weeks. A classification can be made by means of the type of eruption that a system shows, together with their durations and recurrences [55]. This classification will be explained in section 1.1.3.

In this thesis, we are interested in the periods of time in between outbursts rather than the outbursts themselves. During these *quiescent intervals*, we are able to probe the characteristics of the accretion disc surrounding the white dwarf. We are interested in particular in the *linear rms-flux relation* which is associated with *flickering variability* [48, 43]. We will introduce the characteristics of accretion and accretion-induced variability in section 1.2.

We will now discuss CVs in more detail. Section 1.1.1 expands on the mechanisms underlying accretion in binary systems, the formation of the accretion disc and the physics within the disc itself. Section 1.1.2 describes the evolution of CVs and the processes that drive it. The classification system for CVs will be explained in section 1.1.3.

1.1.1 Accretion in binary systems

Compact interacting binaries are binary systems in which matter from the secondary accretes onto the central compact object. This central object can be a white dwarf, neutron star or black hole. A CV is hence a compact interacting binary with a white dwarf as central object. Binary systems with a neutron star or black hole as central object are called *X-ray binaries* (XRBs).

Roche-lobe overflow

Accretion in these binary systems occurs via *Roche-lobe overflow*. In order to explain this mechanism, we need to introduce the *Roche potential*. The Roche potential approximates the total force of the binary acting on a test particle. It is an approximation since it assumes that the orbit of the components of the system is circular and that the components themselves are point masses. CVs, and compact interacting binaries in general, have circular orbits as we will see in section 1.1.2. Its components are not point masses, but are in general sufficiently centrally condensed for this approximation to hold. In a frame of reference rotating with the binary, the Roche potential can be written as

$$\Phi_R(\vec{r}) = -\frac{GM_1}{|\vec{r}-\vec{r_1}|} - \frac{GM_2}{|\vec{r}-\vec{r_2}|} - \frac{1}{2}\left(\omega \times \vec{r}\right)^2,$$

with G the gravitational constant, M_1 and M_2 the masses of the primary and the secondary, and $\vec{r_1}$ and $\vec{r_2}$ the position vectors of their centres. The angular velocity of the binary, relative to an inertial frame, is denoted by ω [19, 12].

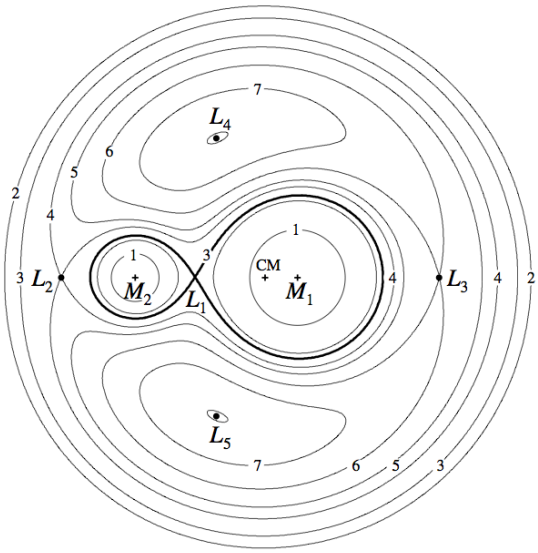

Figure 1.1: The Roche potential of a binary system with a mass ratio $q = 0.25$. Shown are the centres of mass of the primary and secondary (M_1, M_2), the centre of mass of the binary (CM) and the Lagrangian points L_1, L_2 and L_3. L_4 and L_5 are local maxima of the Roche potential. The equipotentials are labelled in order of increasing Roche potential. The heavy line marks the Roche-lobes surrounding the components. Figure from [12].

Figure 1.1 shows a contour plot of the Roche potential for a system with mass ratio $q = M_2/M_1 = 0.25$. The primary of this system is hence four times as massive as its secondary. The contours plotted are equipotential surfaces. The binary system is surrounded by a dumbbell-shaped critical equipotential surface, the part surrounding each component is known as its Roche-lobe. Within the Roche-lobe, the motion of matter is dominated by the gravitational pull of the component. It is therefore the largest equipotential surface that can contain the mass of that component before it becomes unbound. The shape of the Roche-lobes of a binary system is solely determined by its mass ratio. Three physically

meaningful parts of the Roche potential are denoted on figure 1.1: the inner Lagrangian point L_1 and the outer Lagrangian points L_2 and L_3. At the Lagrangian points, the total force acting on the test particle is zero. Matter associated with a star can hence escape from its Roche-lobe via one of these Lagrangian points. The inner Lagrangian point lies in between the Roche-lobes surrounding the binary components and is a saddle point in the Roche potential. In CVs and all other compact interacting binaries, the secondary overflows its Roche-lobe. Matter can hence freely flow over into the Roche-lobe of the primary via the inner Lagrangian point: this process is called *Roche-lobe overflow* [12, 55].

Formation of the accretion disc

As material from the secondary enters the Roche-lobe of the white dwarf via the inner Lagrangian point, it has non-zero angular momentum with respect to the white dwarf. It therefore does not directly accrete onto the surface of the white dwarf. From the viewpoint of the white dwarf, it is as if material escapes through a nozzle rotating around it in the binary plane [12, 55]. This is visualised in figure 1.2.

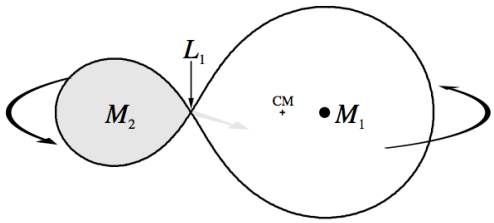

Figure 1.2: Visualisation of Roche-lobe overflow from the secondary to the primary through the inner Lagrangian point L_1. M_1 and M_2 are the masses of the primary and secondary, CM denotes the centre of mass. Figure from [12].

Because the matter has non-zero angular momentum with respect to the white dwarf, it starts orbiting the white dwarf. It follows an elliptical orbit in the binary plane. The presence of the secondary causes this orbit to precess through tidal effects. The stream of matter hence intersects itself, resulting in energy dissipation via shocks. Angular momentum is not dissipated as easily. The matter will therefore tend to the orbit associated with the least energy for its angular momentum: a circular orbit. The white dwarf is now surrounded by a ring of matter [12].

The matter within the ring experiences dissipative processes such as collisions, shocks, and viscous dissipation. These processes convert some of the energy of the bulk orbital motion into heat, which will be partly radiated away. The orbital energy of the ring hence decreases, making the ring spread out to smaller radii (closer to the white dwarf). As a circular orbit has the least energy, the matter spirals slowly inwards to the white dwarf through a series of approximately circular orbits in the binary plane. The spiralling-in of matter implicates a loss of angular momentum. The time scale on which the matter can redistribute its angular momentum is in general much longer than both the time scale on which it loses energy by radiative cooling and the orbital time scale. The matter will hence lose as much energy as possible at a given angular momentum. As no external torques are present, angular momentum can only be lost by internal torques which transfer it

outwards. The outer part of the disc will therefore regain angular momentum and spiral outwards [12, 55].

The original ring will hence have spread out to both smaller and larger radii: the accretion disc has formed. Figure 1.3 illustrates the various processes described above in a schematical way.

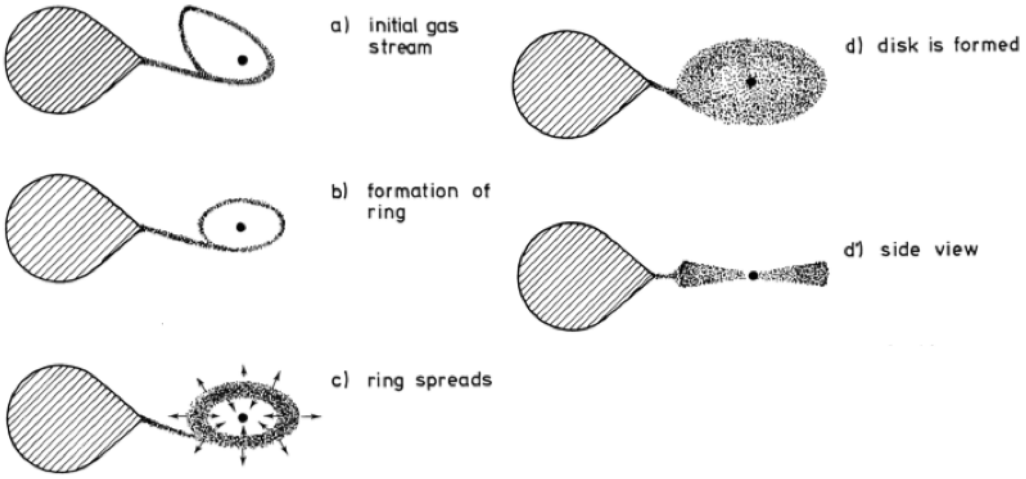

Figure 1.3: Illustration of the initial formation of a ring around the primary and its evolution into an accretion disc. Figure from [52].

Accretion disc physics

In general, we can neglect the self-gravity of the disc as its total mass is sufficiently small and its mean density is much lower than that of the primary and of the secondary. The circular orbits within the disc are therefore Keplerian. These Keplerian orbits imply *differential rotation* within the disc, as the angular velocity of matter depends on the radius of its orbit. Since adjacent rings in the disc move past each other with different velocities, any viscous processes in the flow will generate heat from the shearing flow. As explained in the previous section, the dissipation of the heat generated by viscous processes decreases the orbital energy within the disc, making matter spiral inwards. The angular momentum redistribution associated with this process causes matter to move to larger radii [12, 55].

The viscosity in the disc can be described by the α-formalism of Shakura & Sunyaev (1973). In this formalism, viscosity ν is given by

$$\nu = \alpha c_s H$$

with c_s the speed of sound and H the thickness of the disc. Viscosity is hence linearly proportional to the thickness of the disc, which is related to its total pressure within a Keplerian disc. The α-formalism is a parametrisation of viscosity rather than a physical prescription: everything we do not know about the process is encoded in the viscosity parameter α [44]. The main viscous process at work in the disk is thought to be turbulent viscosity, caused by the turbulent motions of the matter in the disk [19, 55].

At the inner and outer edges of the accretion disc, two interesting features occur: the boundary layer and the bright spot. As the matter approaches the surface of the white dwarf, its velocity remains equal to the Keplerian velocity. When it enters the *boundary layer*, the matter decelerates to the white dwarf's surface velocity. A large amount of energy is released during this deceleration, as much so that the boundary layer can emit up to half of the total luminosity of the system. How the energy is radiated away depends on the optical depth of the boundary layer. For an optically thick boundary layer, the radiation has to diffuse through a distance H within the disc before emerging. Figure 1.4 gives a schematic view of this process. Emission of optically thick boundary layers is typically in the soft X-ray domain. If the boundary layer is optically thin, the radiation can escape directly from the shock front formed where the matter meets the white dwarf's surface. The radiation is emitted at the shock temperature, giving in general rise to hard X-ray emission [55].

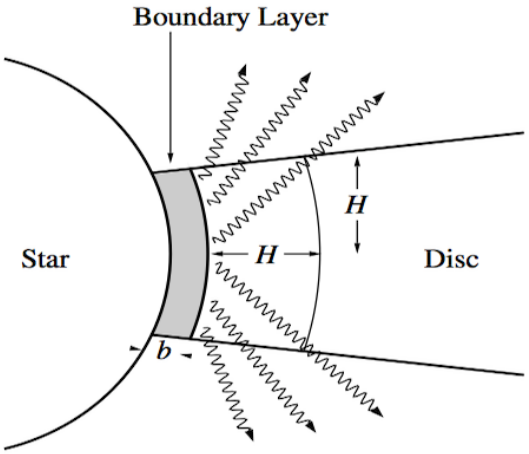

Figure 1.4: Schematic view of an optically thick boundary layer, shown in a plane perpendicular to the disc. Figure from [13].

At the outer edge of the accretion disc, the Roche-lobe overflow of the secondary crashes into the disc. This creates a shock-heated area at the outer rim of the disc, also called the *bright spot*. The bright spot hence also emits radiation, and in some systems it emits more energy at optical wavelengths than the primary, secondary and accretion disc combined [55].

Eruptions and outbursts

We have previously mentioned that we can distinguish between two types of cataclysmic events: nova eruptions and dwarf nova outbursts. *Nova eruptions* are caused by hydrogen-rich matter from the secondary piling up on the surface of the white dwarf. As the matter piles up on the surface and forms a non-degenerate layer, its pressure increases and it subsequently becomes degenerate. The equation of state of degenerate matter is independent of temperature: if the temperature and density of the degenerate layer are high enough for hydrogen fusion to occur, any small increase in temperature leads to runaway hydrogen fusion. The runaway ends when the temperature of the layer is

sufficiently high to end degeneracy. The layer expands to reduce the overpressure: the layer "explodes" [19, 55].

Dwarf nova outbursts are caused by disc instabilities. The energy released originates from the gravitational field of the white dwarf rather than a thermonuclear runaway. During a quiescent interval, the accretion disc has a low viscosity and hence an inefficient exchange of angular momentum. The mass transfer rate through the disc is therefore smaller than the mass transfer rate from the secondary. This results in matter accumulating in the disc, which increases the density and the temperature in one of its annuli. When a critical surface density is reached, the temperature of the annulus is sufficiently high to ionise hydrogen. The ionisation of hydrogen makes the matter transition to a high-viscosity state. This high-viscosity state propagates inward and outward in the disc until the entire disk is in this state. Angular momentum and mass transport now occurs very efficiently through the disc: the accumulated matter in the disc is drained onto the white dwarf, releasing a large amount of gravitational energy [58, 19, 55].

1.1.2 Evolution of cataclysmic variables

CVs are *close* binary systems, meaning that the distance between the components is sufficiently small so that a force additional to the gravitational force governs the system as well. In this case the additional force is the tidal force, which circularises the system's orbit, one of the assumptions made in the Roche potential. Tidal effects also strongly distort the shape of the secondary, making it tear-shaped instead of spherical. CVs are also *semi-detached* binary systems since the secondary overflows its Roche-lobe, which causes an accretion disc to be formed [55].

CVs are close, semi-detached binary systems because of orbital angular momentum loss, causing its components to slowly spiral towards each other. This decrease in orbit is a remnant of the *common envelope* phase of their binary evolution, which we will not expand on as it lies beyond the scope of this thesis. Angular momentum loss hence decreases the separation of the components, making them interact more strongly. Note that as the orbit decreases in size, the orbital period of the system decreases as well.

Initially, the angular momentum loss is caused by *magnetic braking*. For this to occur the secondary needs to have a magnetic field and a stellar wind. The magnetic field is generated by a "dynamo" located between its radiative core and convective envelope. The magnetic field lines can be thought to be frozen in to the bulk of the secondary, making them co-rotate with the star. The secondary's stellar wind consists of hot ionized matter and is hence strongly coupled to the magnetic field. Because of this, the wind gains angular momentum when it moves outwards. When its kinetic energy exceeds the magnetic energy, the wind breaks free and carries off the angular momentum. The strong tidal interaction between the components implies that angular momentum carried away from the secondary reduces the orbital angular momentum of the system [19, 55].

While the orbit of the system is reduced, the secondary loses mass via Roche-lobe overflow. When its mass reaches approximately 0.2 $M_\odot$, the interior becomes fully convective. This destroys the secondary's magnetic field and stops the angular momentum loss via magnetic breaking. The mass loss rate of the secondary is subsequently reduced, causing the secondary to contract and eventually lose contact with its Roche-lobe, stopping mass loss all together. The system, now a detached binary, still loses angular momentum but

via a different mechanism: *gravitational radiation*. At an orbital period of about 3 h, the components are sufficiently close together for gravitational radiation to cause significant angular momentum loss. The orbital period hence continues to decrease. At an orbital period of about 2 h, mass transfer starts again since the secondary's Roche-lobe has shrunk sufficiently for it to overflow again. When the period lies between about 2 and 3 h, the system lacks mass transfer, which decreases the flux emitted drastically and makes the system hard to detect. This range in period is hence called the *period gap* [19, 55, 31].

The decrease in orbital period through angular momentum loss stops when a period of approximately 80 min, also known as the *period minimum*, is reached. The secondary can be characterised by the exponent α of the mass-radius relationship (in solar units). In main sequence stars, α is approximately equal to one. At the period minimum, the α characteristic to the secondary is reduced from its near-main sequence value to 1/3. This is because the severe mass loss it has experienced during the evolution has driven the secondary away from thermal equilibrium. In CVs, the period minimum coincidentally occurs when the secondary star has evolved into a brown dwarf. The CV now consists of two degenerate objects, namely the white dwarf primary and brown dwarf secondary. Since a brown dwarf responds to mass loss by expanding (instead of contracting), the period of the system starts to increase. CVs that have evolved beyond the period minimum are therefore called *period bouncers* [19, 55, 30].

1.1.3 Classification of cataclysmic variables

Several classification systems have been used to order the CV zoo, where the oldest systems merely rely on the general characteristics of the light curve. As new insights into the physics governing CVs and their accretion discs were obtained, many of the old classes had to be merged or redefined [55]. This resulted in a simpler system, which we will briefly discuss.

Classical novae Classical novae (CN) have only one observed eruption. As mentioned in section 1.1.1, the eruption is caused by a thermonuclear runaway of the hydrogen-rich matter of the secondary piling up on the white dwarf's surface. The increase in brightness during the eruption ranges from 6 to 19 magnitudes and is inversely correlated to the duration of the eruption [55].

Dwarf novae The cataclysmic events of dwarf novae (DN) are outbursts which are, as mentioned in section 1.1.1, large releases of gravitational energy. During the outburst, the increase in brightness ranges from 2 to 5 magnitudes. Every system has a well-defined quiescent interval between outbursts, which ranges from a couple of days to several years. The duration of the outburst ranges from 2 to 20 days, and is correlated with the duration of the quiescent interval between them. The dwarf novae consist of three subclasses, based on the morphology of their light curve [55]:

- *SU UMa stars* have occasional superoutbursts. These outbursts are both brighter and longer than the normal dwarf nova outbursts and appear to occur more regularly. We will expand on the origin of superoutbursts in chapter 2.
- *Z Cam stars* have long standstills at about 0.7 times the maximal brightness. Outbursts do not occur during a standstill.

- *U Gem stars* are dwarf novae that are neither SU UMa or Z Cam stars.

Recurrent novae Recurrent novae (RN) are systems that were previously thought to be CN, but have been found to repeat their eruptions. The distinction between DN and RN can be made spectroscopically: during RN and CN eruptions a large shell is ejected, which is not the case during DN outbursts [55].

Nova-like variables Nova-like variables (NLs) include all CVs without outbursts or eruptions. The lack of cataclysmic events is due to the stable rate of mass transfer through their discs. These systems include pre-novae, post-novae and Z Cam stars in permanent standstill [55].

Magnetic CVs In magnetic CVs (mCVs), the white dwarf has a magnetic field. As the accreted matter is hot and ionized, it follows the magnetic field lines of the white dwarf and does not form an accretion disc, either partly or completely. The formation of an accretion disc depends on the strength of the magnetic field: very strong fields force matter to accrete directly onto the magnetic poles of the white dwarf, while more moderate fields only partly disrupt the accretion disc. Even with a partial accretion disc, the behaviour of mCVs differs strongly from non-magnetic CVs [55].

1.2 Accretion-induced variability

Periodic variability (quasi-periodic oscillations and periodic modulations) and aperiodic broadband variability (*flickering variability*) have been observed in compact interacting binaries and in active galactic nuclei (AGN, galaxies with a central accreting supermassive black hole). These types of variability are accretion-induced: they are generated by the flow of matter from the secondary passing through the accretion disc surrounding the central object. Flickering variability has several properties, such as frequency dependent time lags, a lognormal flux distribution and a *linear rms-flux relation* [48, 8, 43]. The rms-flux relation is the main topic of this thesis, which will be introduced in section 1.2.1. The time scale and energy range at which flickering variability can be observed depends on the object: for XRBs and AGN, flickering variability ranges respectively from milliseconds to minutes and from days to years in the X-ray domain, for CVs it ranges from seconds to days in the optical and UV domain. The difference in energy can be explained by the size of the central accreting object: in smaller compact objects, the inner rim of the accretion disc surrounding them is smaller. The material therefore falls much deeper into the gravitational potential well of the compact object, emitting radiation at higher energies. As the radius of a white dwarf is over an order of magnitude larger than that of a neutron star or the Schwarzschild radius of a black hole, XRBs and AGN emit in the X-ray domain, while CVs emit in the optical or UV domain. In smaller compact objects a larger portion of the disc is located at smaller radii, giving the flickering variability a larger high-frequency component. The Schwarzschild radius of a black hole scales linearly with mass, so the inner rim of the accretion disc in AGN is smaller that that in XRBs, which explains the difference in time scales [4, 41].

The properties of flickering variability in XRBs and AGN have been studied in great detail. This is mainly thanks to the NASA *Rossi X-ray Timing Explorer* mission dedicated

to observing in the X-ray domain, which has yielded data suitable for the detection and analysis of flickering variability [23]. Flickering variability has not yet been studied in such detail in CVs as long, uninterrupted high-quality optical data is needed in order to study flickering variability in these systems. The launch of the NASA *Kepler* mission in 2009 has provided the scientific community with enormous amounts of such data, hence facilitating CV research [41]. We will discuss the *Kepler* mission in chapter 3. Figure 1.5 shows a quiescent interval in the *Kepler* light curve of V1504 Cyg, one of the CVs that will be studied in this thesis. Flickering variability is clearly visible during this quiescent interval.

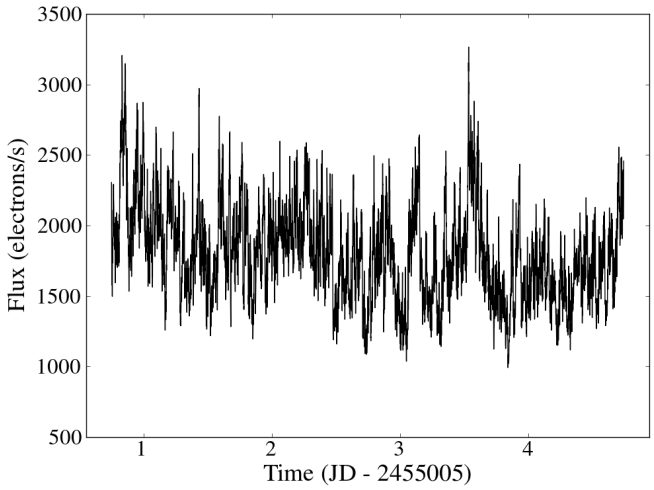

Figure 1.5: A quiescent interval in the *Kepler* light curve of V1504 Cyg. Flickering variability is clearly visible throughout the interval. The average error is equal to 20.3 electrons/second and is therefore not visible in the plot.

1.2.1 The linear rms-flux relation

The linear rms-flux relation is the property of flickering variability on which we will focus in this thesis. The relation relates the absolute root-mean-square (rms) variability amplitude of the light curve to its flux in a linear way: the stronger the variability, the brighter the system [48].

Together with the lognormal flux distribution, the rms-flux relation implies that the short and long time scales of flickering are coupled. The coupling of time scales is important when modelling flickering variability. It is achieved by multiplying all variations, where the variations occur over all time scales. This is done in the *fluctuating accretion model*, which will be expanded on in chapter 2. When all variations are added together, as is done in the *shot noise model*, the time scales are not coupled. The rms-flux relation is hence not present, and the flux distribution will be normal instead of lognormal [4].

The rms-flux relation was first discovered in the X-ray light curves of the black hole XRB Cyg X-1 and the neutron star XRB SAX J1808.4-3658 is by Uttley & McHardy in 2001. The light curves used were obtained by the *RXTE* mission and have a length of 18 ksec and 23 ksec respectively. Figure 1.6 shows the rms-flux relations found in these systems [48].

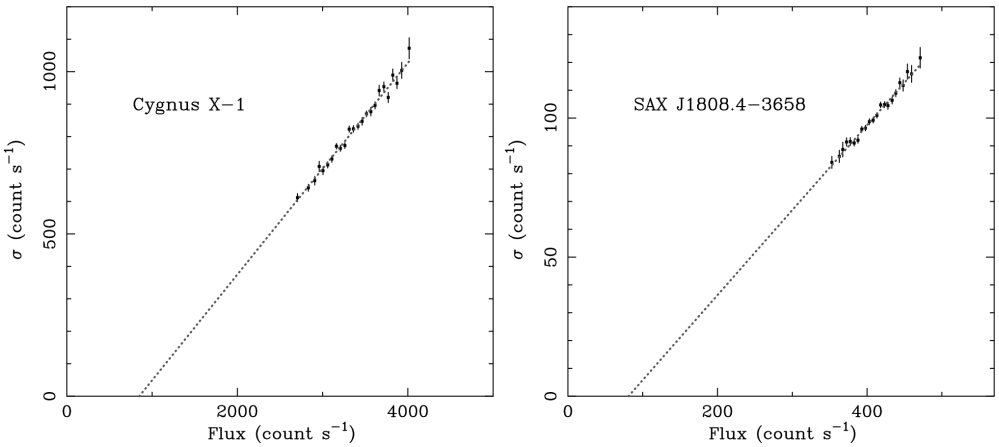

Figure 1.6: The rms-flux relation detected Cyg X-1 and SAX J1808.4-3658, using *RXTE* light curves of respectively 18 ksec and 23 ksec. The dotted lines mark the best-fit models. Figure from [48].

1.2.2 Universal nature of accretion-induced variability

It is thought that the physics governing accretion onto compact objects is independent of the type, mass or size of the central accreting object. In other words, accretion onto compact objects is thought to be universal. This hypothesis is built on the similarities detected in the accretion-induced variability observed in XRBs, AGN and CVs [43, 39].

Both periodic variability and aperiodic flickering variability have been observed in all these systems. However, because of the availability of high-quality X-ray data, the characteristics of flickering variability have been studied in more detail only for XRBs and AGN. More specifically, the rms-flux relation has been found in multiple XRBs and AGN [48, 51, 15]. With the advent of the NASA *Kepler* mission, large amounts of high-quality data suitable for its detection in CVs are now available. Nonetheless, so far only one CV has been shown to exhibit the rms-flux relation: MV Lyrae. In figure 1.7, the rms-flux relation detected in this system is shown. Scaringi et al. (2012) used a *Kepler* light curve spanning 10 days for its detection [43].

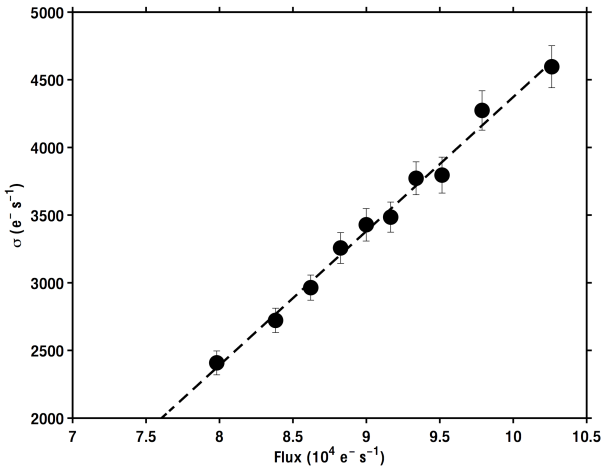

Figure 1.7: The rms-flux relation detected in MV Lyrae, using a *Kepler* light curve of 10 days. The dotted line marks the best fitted model. Figure from [43].

The aim of this thesis is to detect the rms-flux relation in as many CVs in the *Kepler* field-of-view as possible. Its detection in other CVs would effectively enforce the hypothesis of the universal nature of accretion-induced variability. In chapter 2, we will expand on both the periodic and aperiodic component of accretion-induced variability. The selection of the CVs that will be analysed and the collection of their *Kepler* data will be discussed in chapter 3. The methods used to analyse the data will be explained in detail in chapter 4. The results of the data analysis will be given in chapter 5. These results will be discussed in chapter 6.

Chapter 2

Accretion-induced variability in binary systems

In this chapter we will expand on the nature of accretion-induced variability in compact interacting binary systems and its origin. Before we can do so, we will discuss the techniques used to examine time series in section 2.1. We then continue with discussing and simulating the several types of noise relevant to this thesis in section 2.2. Accretion-induced variability can be split into a periodic and an aperiodic component. In section 2.3, we will discuss the periodic component. The aperiodic component, also known as flickering variability, will be discussed in section 2.4.

2.1 The power-spectral density function

Consider a time series composed of multiple signals, each with their own specific frequency. The *power* of a signal tells us how much this signal contributes to the total power of the time series. This can be estimated with the *power-spectral density function* (PSD), which describes the distribution of power as a function of frequency f. We will use Fourier techniques to examine time series. By using these techniques we inherently assume that the time series can be modelled by multiple sinusoids. Note that when using Fourier techniques, we are working in the frequency-domain instead of the time-domain.

The PSD is calculated as the squared modulus of the discrete Fourier transform of the time series $x(t)$:

$$PSD(f) = \frac{1}{N} |\sum_{t=1}^{N} x(t)\ e^{2\pi i f t}|^2,$$

with N the number of data points [47]. The PSD is then normalised using the *rms-normalisation*, in which the PSD is divided by the square of the mean flux level of the time series. This specific normalisation is used so that the square root of the PSD integrated over a specific frequency range gives us the fractional rms (root-mean-square) variability in this range. The units of the PSD in the rms-normalisation are $(\text{rms/flux})^2/\text{Hz}$. [5, 34, 43].

Periodic and aperiodic processes in a time series give rise to distinctly different PSDs. An example of a periodic process is the orbit of a binary system. Depending on the inclination angle at which the system is observed, this can give rise to a periodic signal in its light curve with a frequency corresponding to the orbital period. The PSD of a time series including such a periodic process would show a finite number of peaks,

corresponding to the frequency of the process and its harmonics. Harmonics are present when a single periodic signal needs to be described by multiple sinusoids. Examples of aperiodic processes are noise and flickering variability. The PSD of a time series including an aperiodic process is a smooth function of frequency [47]. In the following section, various examples of PSDs will be given.

2.2 Types of noise

In this section, we will describe and simulate three types of noise: white, red and zero-centred Lorentzian-shaped noise. The simulations are performed using the algorithm of Timmer & König (1995), hereafter T&K, in the programming language Python [22]. After specifying the PSD-shape, the T&K algorithm simulates a time series that displays the desired PSD-shape. The time series produced is only one of all possible time series that satisfy this condition. The T&K algorithm consists of the following steps [47]:

- Specification of the desired PSD-shape that the simulated time series should display and of the number of Fourier frequencies, i.e. the frequencies in the Fourier domain, that need to be generated. The Fourier frequencies to be used are evenly spaced between 0 and 1 Hz.
- For each frequency f, two standard normal distributed random numbers are chosen, which are then multiplied by $\sqrt{\frac{1}{2}\ PSD(f)}$, with $PSD(f)$ the desired PSD shape. The result is used as the real and imaginary part of the Fourier transform of the to-be-simulated time series.
- In order to obtain a real-valued time series, the Fourier components of the negative Fourier frequencies are chosen to be the complex conjugate of the previously obtained Fourier transform. The Fourier components of the positive Fourier frequencies are chosen to be equal to the Fourier transform.
- The time series is obtained by inverse discrete Fourier transformation.

We will convert the units of frequency and time to realistic units for *Kepler* data. This is done by multiplying the initial Fourier frequency range with half the *Kepler* short cadence sampling interval. Chapter 3 will expand on the short cadence sampling and other characteristics of the *Kepler* mission. The unit of flux could be converted to a realistic unit for *Kepler* data by adding the average flux observed in the *Kepler* light curves of the CVs analysed in this thesis to the generated time series. However, the average flux observed depends on the brightness of the object and other factors, which will be discussed in chapter 3. We will hence keep the "virtual" unit of flux, relative counts, as the main objective of the simulations is to visualise noise time series and their PSDs rather than to simulate realistic *Kepler* light curves. Note that the PSDs obtained for a simulated time series will not be rms-normalised.

2.2.1 White noise

White noise is essential to all astronomical observations. It is mainly an inconvenience as it is mostly caused by instrumental Poisson noise. Poisson noise differs from white noise, but this difference decreases with increasing number of measurements. Given the extent of the *Kepler* data sets we will analyse, we can say that Poisson noise is equal to white

noise [16]. The general shape of the PSD of white noise is flat. The PSD is therefore very simple [47]:

$$PSD(f) = constant\,.$$

In figure 2.1, a white noise time series and its corresponding PSD simulated by the T&K algorithm are shown. In the simulation, the constant has been given a value of 1. The flat shape of the PSD is clearly visible in figure 2.1b.

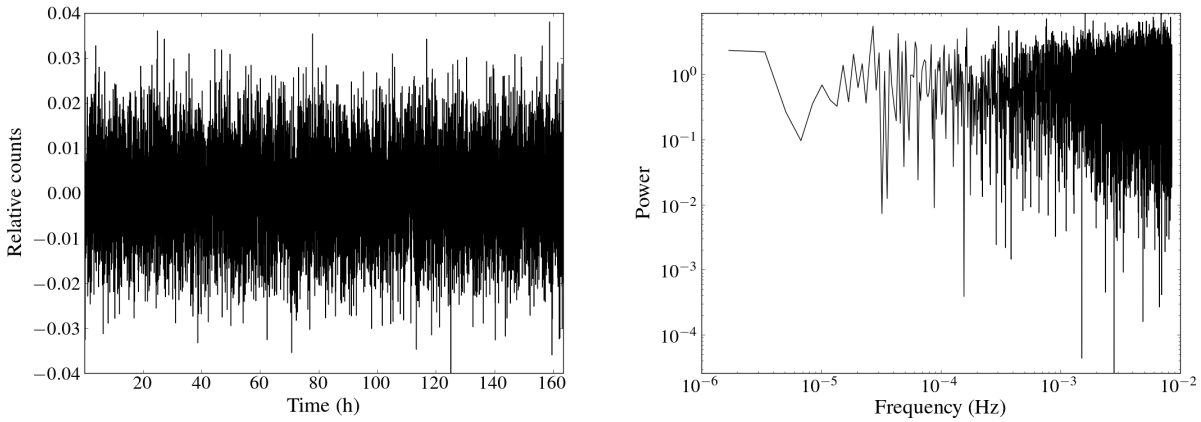

(a) Time series (b) PSD

Figure 2.1: Simulated white noise time series and its corresponding PSD.

The level of Poisson noise of a light curve can be estimated when calculating its PSD in the rms-normalisation. Using this normalisation, the level of Poisson noise P of a *Kepler* light curve $x(t)$ is given by

$$P\left(x(t)\right) = 2\left(\frac{1}{N}\sum_{i=1}^{N} x_i(t)\right)^{-1},$$

where N is equal to the number of data points out of which the light curve $x(t)$ consists. It has the same units as the rms-normalised PSD [5, 34, 43].

2.2.2 Red noise

The PSD of red noise is given by [47]:

$$PSD(f) \sim \frac{1}{f}\,. \tag{2.1}$$

For the T&K simulation of red noise, we choose the proportionality constant to be equal to one. The simulated time series and its corresponding PSD are shown in figure 2.2. Figure 2.2b clearly shows the $1/f$ relation in the PSD. Red noise is an approximate way to model flickering variability; its PSD-shape approximates the PSDs observed of XRBs, AGN and CVs [48, 42].

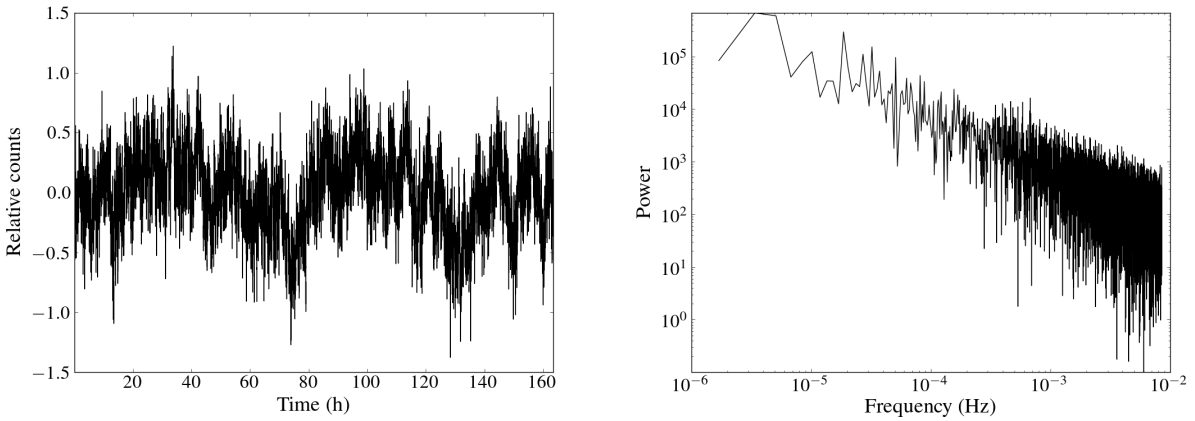

(a) Time series (b) PSD

Figure 2.2: Simulated red noise time series and its corresponding PSD.

2.2.3 Zero-centred Lorentzian-shaped noise

Zero-centred Lorentzian-shaped noise is named after the shape of its PSD, which is a zero-centred Lorentzian in function of frequency. The Lorentzian is characterised by its break-frequency f_b. The shape of the PSD will be equal to the PSD of red noise for frequencies below f_b, with a slope of -1. For frequencies above f_b the slope will be -2, the break frequency hence "kinks" the PSD. The PSD of zero-centred Lorentzian-shaped noise is given by [6]:

$$PSD(f) \sim \frac{1}{f\left(1+\frac{f}{f_b}\right)}.$$

We will again choose the proportionality constant to be equal to one in the T&K simulation. Two time series and their corresponding PSDs with different break frequencies have been simulated: in figure 2.3 the simulated noise has a break frequency of 10^{-3} Hz, in figure 2.4 it has a break frequency of 10^{-4} Hz. The break frequency has a physical meaning, which will be discussed in section 2.4. Zero-centred Lorentzian-shaped noise can also be used to model flickering variability [42].

The break frequency has an effect on both time series and PSD. In the PSDs, figures 2.3b and 2.4b, the "kink" is clearly located at their respective break frequency. Note that the PSDs are now plotted as power $\times$ frequency instead of power. This is done so that the "kink" caused by the break frequency is more noticeable. The time series, figures 2.3a and 2.4a, show more variability for a higher break frequencies.

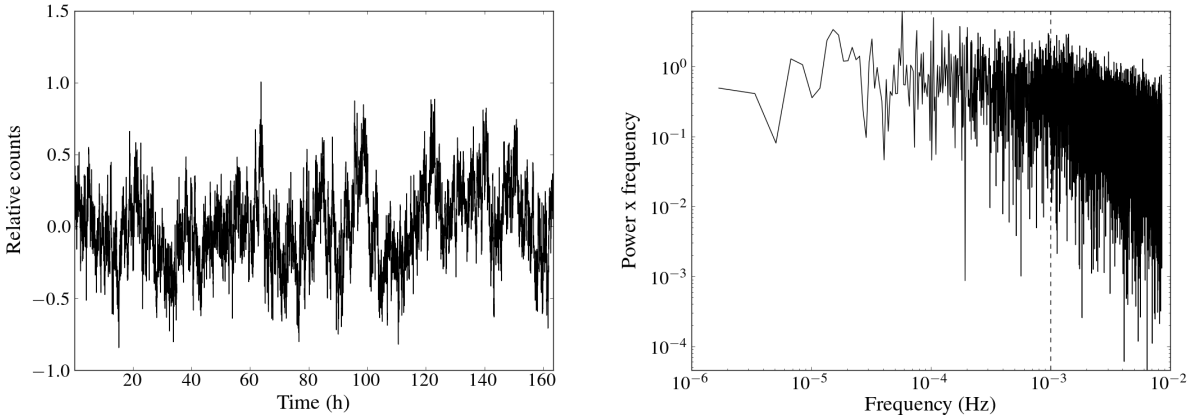

(a) Time series (b) PSD

Figure 2.3: Simulated zero-centred Lorentzian-shaped noise time series with break frequency 10^{-3} Hz and its corresponding PSD. The dashed line marks the break frequency.

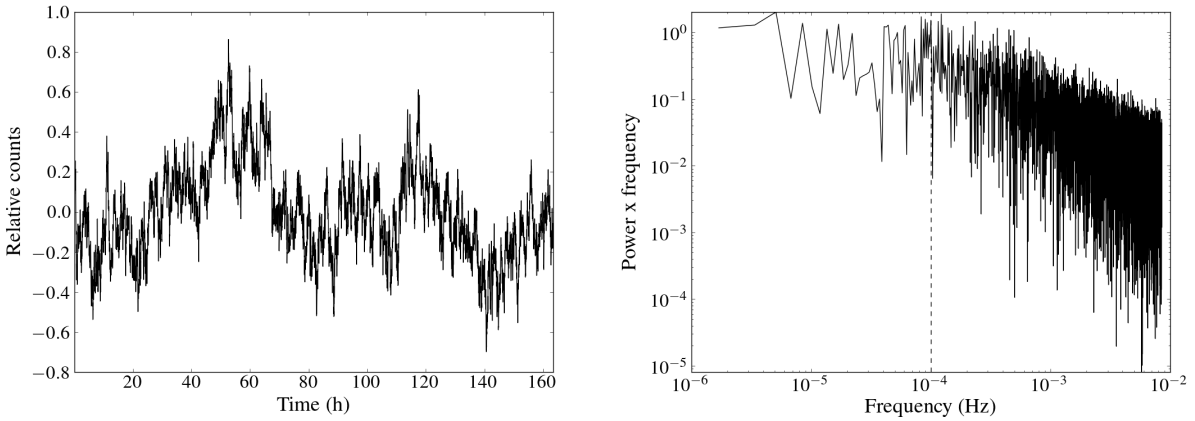

(a) Time series (b) PSD

Figure 2.4: Simulated zero-centred Lorentzian-shaped noise time series with break frequency 10^{-4} Hz and its corresponding PSD. The dashed line marks the break frequency.

2.3 Periodic variability

As previously mentioned, accretion-induced variability has both a periodic and an aperiodic component. Both components of accretion-induced variability, together with their respective characteristics, have been observed in XRBs, AGN, and CVs. These observations play a large role in the hypothesis of the universal nature of accretion-induced variability.

Various periodic phenomena can be categorised as periodic variability. In this section, we will discuss three types of periodic variability that differ both in origin and manifestation in the light curve: quasi-periodic oscillations, superhumps and superoutbursts [19]. The aperiodic component of accretion-induced variability will be discussed in the next section.

2.3.1 Quasi-periodic oscillations

Quasi-periodic oscillations (QPOs) are periodic modulations with periods ranging over 100s of seconds, observed in the light curve of certain CVs. These modulations vanish after a couple of periods, hence their name, and are characterised by a low coherence [53, 7]. A signal is coherent when its phase is constant in time, which gives rise to a clear peak in the PSD located at the signal's frequency. In an incoherent signal, its phase changes with time. As the incoherence increases, the peak in the PSD spreads out over a wider range of frequencies. It is their poor coherence that makes QPOs difficult to detect. Generally 5 to 10 moderately coherent QPO cycles are observed to be clearly visible, before their characteristics change or they disappear altogether [54]. Figure 2.5 shows a QPO with a period of 185 s observed in the CV WX Hyi. A sinusoidal least-squares fit to the light curve is superimposed on the light curve [54].

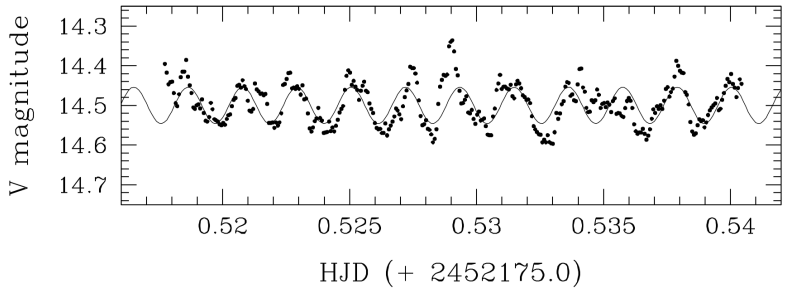

Figure 2.5: Light curve of the CV WX Hyi, showing a QPO with a period of 185 s. The result from the sinusoidal least-squares fit is superimposed. Figure from [54].

There appear to be several kinds of modulations: modulations with almost constant periods and frequent large changes in phase, some of them with a clear growth and decay in amplitude between the phase jumps, and modulations whose period and amplitude constantly vary over a limited range. However, a classification of QPOs has not yet been made as the aperiodic flickering variability hampers their analysis. Several possible mechanisms may be responsible for these modulations. One of the possible mechanisms are non-radial oscillations of the secondary, which causes a modulation in the mass accretion rate. Also, some QPOs have periods comparable to the rotation period of the outer edge of the disk, but no model has yet been proposed for these modulations [19, 12, 55, 53].

2.3.2 Superoutbursts and superhumps

Superoutbursts and superhumps are phenomena that occur in SU UMa stars, a subclass of the dwarf novae. These systems hence also experience normal DN outbursts. *Superoutbursts* are both brighter and longer than normal outbursts and appear to occur more regularly. During a superoutburst, the light curve shows hump-shaped modulations: *superhumps*. These appear near the maximum of the superoutburst and continue until the system has returned to its quiescent state. Superhumps have a period slightly longer or shorter than the orbital period [19].

During a normal outburst, all the excess mass in the disc is dumped onto the white dwarf, so that the disc after the outburst is similar to the disc before. This is not the

case in SU UMa stars: after every normal outburst, the disc grows more massive and expands to larger radii because of angular momentum transport. The disc continues to grow until it has become large enough for the secondary to distort it via tidal effects. The tidal distortion causes the disc to become unstable at a 3:1 resonance. At the 3:1 resonance, the material in the disc completes its orbit around the WD three times for every orbital cycle. These tidal instabilities deform the disc to an elliptical shape and cause it to progradely precess along its long axis. The oscillation of the disc at a 3:1 resonance forms tidal bulges within the disc. When the secondary sweeps by such a tidal bulge, its material gets compressed, causing collisions within the material and hence energy dissipation. These increases in brightness of the disc are the *positive superhumps* and have a period slightly longer than the orbital period. If the disc is tilted in the orbital plane, it does not only precess about its long axis. The disc now also precesses about its node, which is the intersection of the disc with the orbital plane. This is a retrograde precession, causing the *negative superhumps* to have a period slightly shorter than the orbital period. [19, 58, 55].

Because of the elliptical deformation of the disc, the tidal torques within the disc greatly increase its angular momentum transport, which in turn increases the mass flow through the disc. The matter that has been built up after several normal outbursts gets dumped on the white dwarf; this is the *superoutburst* [19, 58]. In figure 2.6, the *Kepler* light curve of the SU UMa star V344 Lyr is shown. Both normal outbursts and superoutbursts are clearly visible.

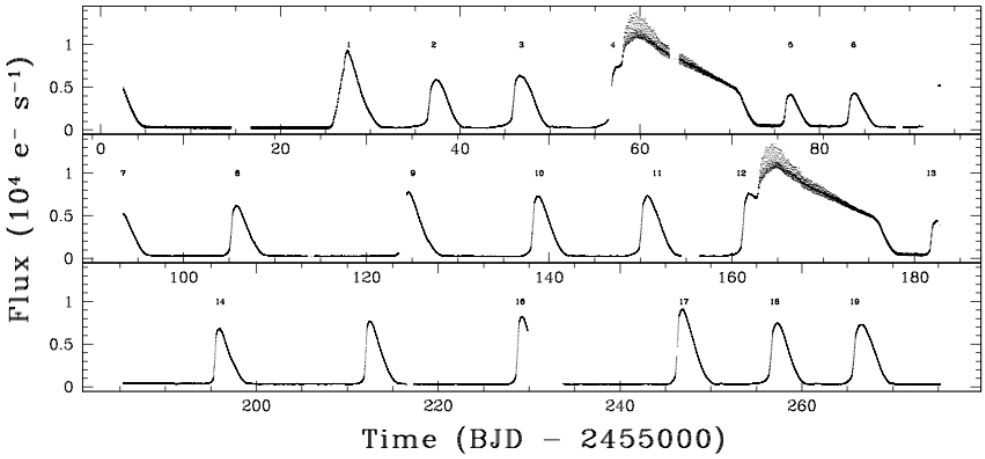

Figure 2.6: *Kepler* light curve of V344 Lyr showing both normal outbursts and superoutbursts. The outbursts are labelled from 1 to 19. Figure from [58].

2.4 Aperiodic flickering variability

Aperiodic flickering variability can be modelled by using a simple power law, such as red noise, or by using zero-centred Lorentzian-shaped noise. Figure 2.7 shows the rms-normalised PSD of all quiescent intervals in the fourth *Kepler* quarter of observations combined of V1504 Cyg. When we compare it to the simulated PSD of red noise and Lorentzian-shaped noise (figures 2.2b, 2.3b, and 2.4b), we can deduce that models using

zero-centred Lorentzian-shaped noise will be more appropriate than those using red noise [41].

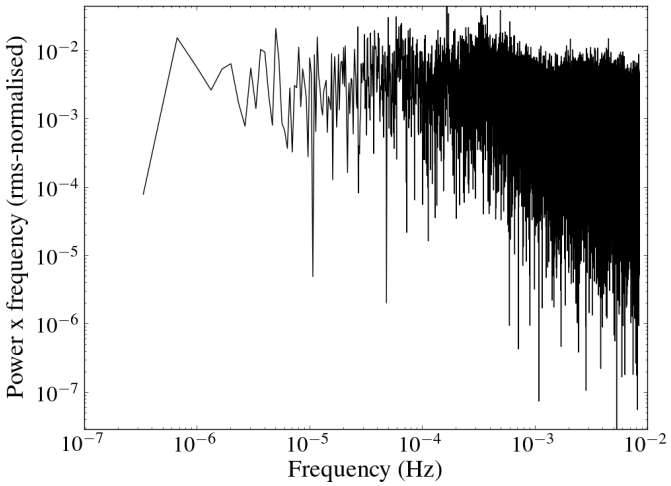

Figure 2.7: Rms-normalised PSD of all quiescent intervals in the fourth *Kepler* quarter of observations of V1504 Cyg combined.

Besides its PSD shape, flickering variability has several other characteristics such as frequency-dependent time lags, a lognormal flux distribution and of course the linear rms-flux relation [50, 49, 8, 41]. When one models the accretion disc surrounding the accreting object, all characteristics of flickering variability have to be taken into account and need to be reproduced by the model. Flickering variability is currently best modelled by the *fluctuating accretion model* [4, 39]. We will expand on the details of this model and explain why it is favoured in the following section.

2.4.1 Fluctuating accretion model

Flickering variability shows large-amplitude variations both on short and long time scales. According to accretion theory, the bulk of the emission of the disc originates close to the central object. This is supported by the observation of large amplitude variations at short time scales. However, large amplitude variations at time scales orders of magnitudes larger than the viscous time scale of the inner disc are observed as well, which suggests that these variations originate at larger radii within the disc. It is this discrepancy in origin that motivated the *fluctuating accretion model*. In the fluctuating accretion model, the bulk of the emission of the disc is produced at the inner boundary layer, while flickering variability originates throughout the disc and modulates the central emission. Flickering variability can hence originate over a wide range of radii, explaining the wide range of time scales on which it appears [33, 32, 4].

The main assumption of the model is a fluctuating accretion flow throughout the disc. The time scales of the fluctuations in the accretion flow are related to the viscous time scale within the disc at their radius of origin. Every independent annulus within the disc, consisting of radii over which the time scales are uncorrelated, hence produces a pattern of fluctuations, $\dot{m}(r,t)$, which has the most variability power at the local viscous frequency

of their radius of origin. The local viscous frequency f_{visc} is given by

$$f_{visc}(r) = r^{-\frac{3}{2}} \left(\frac{H}{R}\right)^2 \frac{\alpha}{2\pi},$$

with (H/R) the ratio of the disc height to its radius, α the viscosity parameter and r the radial position in units of gravitational radii. These accretion rate fluctuations are modelled by Lorentzian-shaped noise with the break frequency corresponding to the local viscous frequency.

Another essential part of the model is that all accretion flow fluctuations are coupled together multiplicatively as they travel towards the white dwarf. When we divide the accretion disc into discrete annuli, the accretion rate at a given annulus $\dot{M}(r_i, t)$ is therefore given by

$$\dot{M}(r_i, t) = \dot{M}_0 \prod_{j=1}^{i} (1 + \dot{m}(r_j, t))$$

with $\dot{M}_0$ the accretion flow leaving the inner Lagrangian point L_1. The outer annulus of the disc corresponds to r_1. The accretion rate at a given annulus is hence given by the multiplication of the contribution to the fluctuations of the annulus itself with the contribution of its outer neighbouring annulus. This annulus in turn includes all fluctuations of all the outer annuli [4].

The fluctuating accretion model reproduces all characteristics of flickering variability. Not only does the model reproduce the shape of the PSD and the linear-rms flux relation, the multiplicative coupling of the accretion flow fluctuations naturally produces a lognormal flux distribution [4, 49].

The predecessor of the fluctuating accretion model, the *shot-noise model*, is based on the additive combination of flares or shots within the accretion disk. This model reproduces the PSD of flickering variability, but fails in reproducing both the rms-flux relation and the lognormal flux distribution. The rms-flux relation and lognormal flux distribution imply that the short and long time scales of flickering variability are coupled, which cannot be achieved through the addition of variations [49].

Chapter 3

Object selection and data collection

In this chapter, we will expand on how we selected the CVs that will be investigated and the data collection process. As we are working with *Kepler* data, a small introduction to the mission and its characteristics will be given as well.

3.1 NASA *Kepler* mission

The NASA *Kepler* mission was successfully launched on March 7 2009. Its main objective was the discovery of Earth-sized exoplanets in and near the habitable zone of Sun-like stars. The habitable zone of a star is the region in which planetary temperatures are suitable for water to exist on the planet's surface [18].

The *Kepler* satellite carries a telescope with a 0.95-metre aperture and a photometer consisting of an array of 42 CCD cameras arranged in 21 modules. It is pointed towards the same field-of-view (FOV) at all times [14]. The FOV, together with the 21 modules, is visualised superimposed on the night sky in figure 3.1. *Kepler* was launched in an Earth-trailing heliocentric orbit. In order for the solar arrays to stay illuminated and for the focal plane to stay pointed away from the Sun, the satellite must be rolled by 90° about its axis approximately every three months. The period of time between two rolls is therefore called a *quarter* (Q).

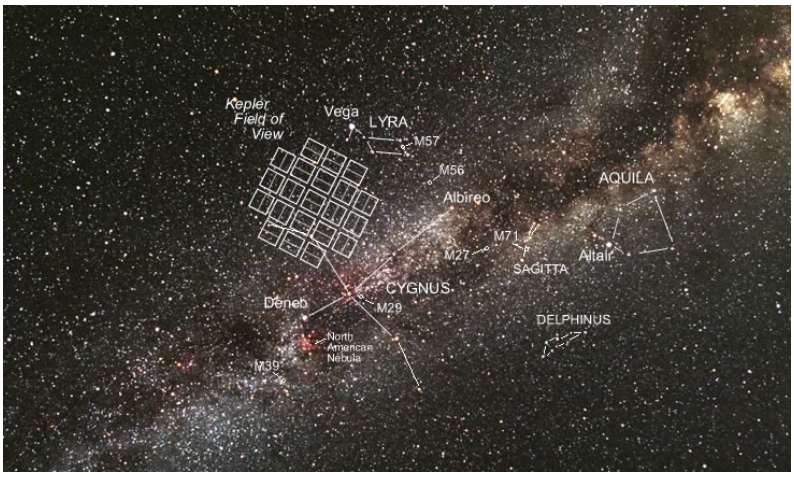

Figure 3.1: The *Kepler* field-of-view superimposed on the night sky. By Carter Roberts, from http://kepler.nasa.gov/multimedia/Images/photogallery/

Kepler can observe up to 150,000 objects simultaneously. Every object has a unique *Kepler* Input Catalogue (KIC) number. Light curves are obtained in two cadences: in *long cadence*, the sampling interval equals approximately 29.4 min whereas in *short cadence*, the sampling interval equals approximately 58.8 s. Not every object is observed at both cadences; more objects are observed at long cadence [18]. NASA's Science Operation Centre provides two calibrated light curves for every object each quarter at every observed cadence: *single aperture photometry* (SAP) and *pre-search data conditioning module* single aperture photometry. The latter is produced specifically to search for exoplanets: signatures correlated with systematic error sources are removed, while preserving the signature of planet transits. This might lead to the removal of flickering variability in the light curves of CVs [16]. We will therefore use the less processed SAP light curve in this thesis. The light curves obtained by *Kepler* are housed in the Archive at the Space Telescope Science Institute and can be downloaded from the Mikulski Archive for Space Telescopes (MAST) [18, 14]. The fast photometric cadence in short cadence mode, the continuous monitoring and the high photometric accuracy of *Kepler* make the short cadence SAP data ideal for observing flickering variability in CVs [40].

Unfortunately, *Kepler* entered a prolonged safe mode in May 2013 where it does not record any data. In order to perform the quarterly rolls and to stabilise the pointing to the single FOV, *Kepler* needs at least three of its four reaction wheels. In May 2013, a second reaction wheel had failed. Nevertheless, the satellite is not lost: the *K2* mission uses solar photon pressure to stabilise the two-wheel satellite. This implies that it is now limited to pointing near the ecliptic plane and it cannot observe a single FOV any more: the *K2* mission observes a sequence of fields as it orbits the Sun. The *K2* mission became operational in June 2014 [20, 46]. From the point of view of CV research, the *K2* mission is an improvement as high quality data will be available for more CVs.

3.2 Object selection

Even though the *Kepler* mission's main objective was the discovery of exoplanets, some CVs can be found in the input catalogue. Our search for CVs in the FOV was based on the paper by Still et al. (2010). There, the authors listed all objects that are found both in the input catalogue and the CV catalogue made by Downes et al. (2001) [45, 9]. Additions to Still's list were made by Williams et al. (2010), Feldmeier et al. (2011), Ramsay et al. (2012) and Ramsay et al. (2014) [57, 11, 37, 36]. Howell et al. (2013) checked spectroscopically if these objects were indeed CVs, checking four more objects at the same time [21].

We have used the MAST archive to find *Kepler* data on the objects listed in the papers mentioned above. Only objects for which short cadence data is available were selected. Table 3.1 contains all objects that will be analysed in this thesis. Together with the nova-like variable MV Lyrae, this table lists all known CVs in the *Kepler* field-of-view for which short cadence *Kepler* data is available. As KIC numbers are easily confused, we will use the object's name as it is listed in the General Catalogue of Variable Stars [38]. One object is not listed in this catalogue, and for this object we will use its KIC number as name. Note that all CVs listed are non-magnetic. Flickering variability is generated in the accretion disc, and mCVs do not always have an accretion disc: it is either absent or

formed only partially. Their behaviour hence strongly differs from that of non-magnetic CVs (see also section 1.1.3). No mCVs were found in the *Kepler* FOV.

Name [38]	KIC number	Type	*Kepler* magnitude	Source
BOKS 45906	9778689	DN	19.046	[11, 36]
V344 Lyr	7659570	SU UMa	14.881	[29, 45, 58]
V363 Lyr	7431243	SU UMa	16.672	[36]
V447 Lyr	8415923	U Gem	18.430	[37]
V516 Lyr	2436450	DN	18.798	[21, 28]
V585 Lyr	5523157	SU UMa	19.489	[21, 28]
V1504 Cyg	7446357	SU UMa	15.805	[35, 59]
	8751494	NL	16.269	[57, 27]

Table 3.1: All CVs under consideration in this thesis. The nova-like variable MV Lyrae is not included, as it has been studied by Scaringi et al. (2012) [43].

3.3 Data collection: selection of quiescent intervals

We will now expand on the collection of data for all CVs listed in table 3.1. For every CV listed in table 3.1, all short cadence SAP *Kepler* light curves available on the MAST archive are downloaded. As we wish to detect the rms-flux relation in as many CVs within the *Kepler* FOV, we need to analyse the quiescent intervals in the light curves of all CVs under consideration. Any outbursts or eruptions present in the light curve need to be neglected: these events dominate the light curve, making it very difficult to probe flickering variability and therefore detect the rms-flux relation.

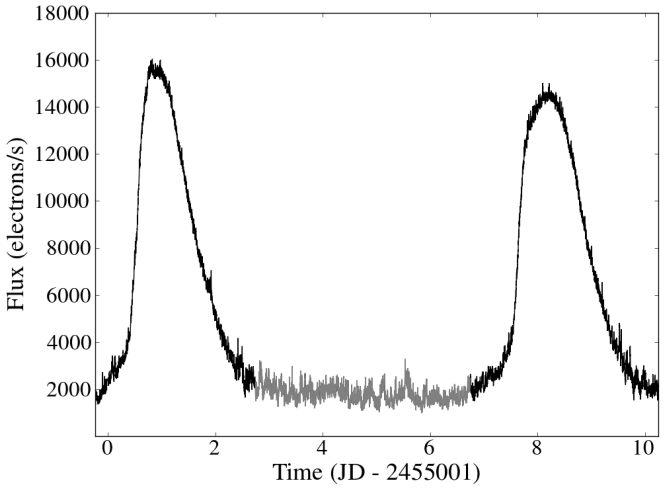

Figure 3.2: Selection of a quiescent interval of V1504 Cyg. The selected quiescent interval is plotted in gray and can also be seen in figure 1.5. The average error is equal to 21.5 electrons/s and is therefore not visible in the plot.

The selection of quiescent intervals between dwarf nova outbursts or nova eruptions has been done by eye: all light curves have been visually inspected in order to determine the start and end of each quiescent interval. An example can be seen in figure 3.2. This figure shows a part of the light curve of V1504 Cyg, with two dwarf nova outbursts clearly visible. The selected quiescent interval is plotted in gray. For the detection of the rms-flux relation, it is very important that the outbursts are not included, as this influences the flux distribution and hence also the rms-flux relation. In order to ensure that the system was fully in its quiescent state, we have used conservative ranges for the selection of quiescent intervals.

Table 3.2 lists the data available for each object. Both the total data, which includes outbursts and eruptions, and the data in quiescent intervals are listed. The number of quiescent intervals and the quarters over which they are observed are listed as well. Quiescent intervals observed in the same quarter can be combined into a single data set, increasing the total number of available data sets for each object with the number of quarters. We cannot combine the quiescent intervals over all quarters, as there are jumps in the mean flux level in between quarters. These jumps are due to *Kepler* entering safe mode during the quarterly rolls, after which the instrument needs to point and be calibrated again. Moreover, the objects move from detector to detector after each roll-over, which also plays a role [25].

Note that for three objects, the total data is equal to the quiescent data. For KIC 8751494, this is because the object is a nova-like variable and hence does not show any outbursts. The SU UMa stars V363 Lyr and V585 Lyr do not display any outbursts during their observations. These objects have "quiescent quarters" instead of quiescent intervals: the number of data sets is equal to the number of quarters.

Object	Total data (d)	Quiescent data (d)	# Quiesc. states	Quarters
V1504 Cyg	1316	549.4	121	2-16
KIC 8751494	226.5	226.5	-	2-3, 5, 15
BOKS 45906	434.0	319.4	6	6-8, 11, 15
V344 Lyr	1343	111.1	37	2-17
V363 Lyr	5.210	5.210	-	16
V447 Lyr	608.8	516.5	16	8-11, 13-17
V516 Lyr	163.0	88.03	11	8-9
V585 Lyr	191.1	191.1	-	9, 14

Table 3.2: *Kepler* short cadence data available for the CVs listed in table 3.1 in the FOV. The length of the total data set is listed. When applicable, the total amount of quiescent data is given, together with the number of quiescent states. The quarters during which the data was collected are listed as well.

3.3.1 Removal of outliers

Outliers are unfortunately always a part of astronomical observations. For example systematic errors, such as pointing drift and focus changes, are one of their many possible causes [16, 14]. Irrespective of their cause, all outliers need to be identified and removed before analysing the data.

As light curves produced by flickering variability are very noise-like, only extreme outliers can be identified by eye. Moreover, the total amount of data for the eight objects is so large that this time-consuming method would not be feasible. Sigma clipping is another possible way to detect outliers, but we have opted for a more visual method of identifying the outliers. For every quiescent interval, the flux distribution has been plotted on a semi-log scale. Using this scaling, any discrepancies to the flux distribution can be spotted more easily. These discrepancies correspond to the outliers in the data set. By visually inspecting the flux distribution of each data set, we can hence determine the range in flux without outliers and remove any measurements outside this range. An example is shown in figure 3.3, in which the outliers of a quiescent interval of V1504 Cyg are determined. This method has of course its disadvantages: the identification of outliers is not quantified, and the determination of the outlier-free flux range is still done visually. However, we have used this method to remove the outliers in all quiescent intervals since it is faster and more accurately detects outliers than visually inspecting the light curve.

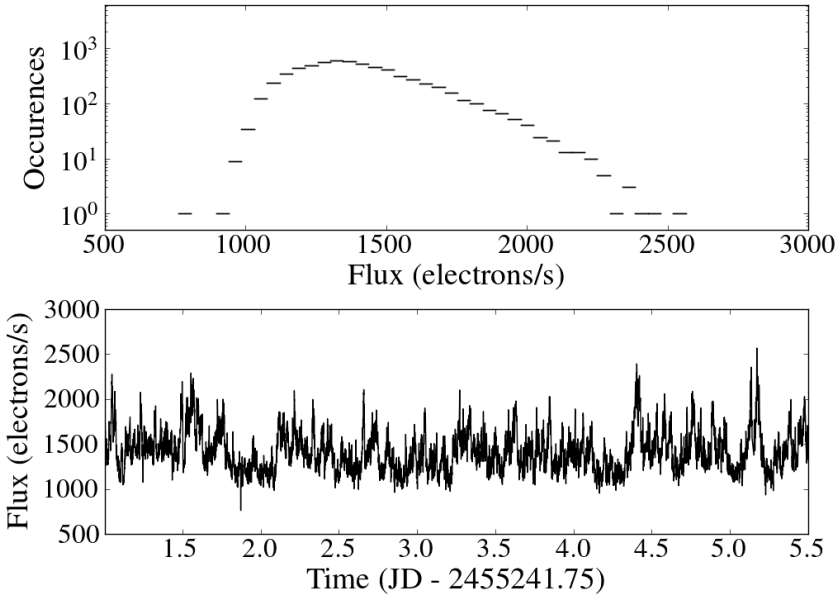

Figure 3.3: Outlier identification in a quiescent interval of V1504 Cyg. The lower panel shows the quiescent interval, the upper panel shows a semi-log plot of its flux distribution. There are clearly a few outliers below a flux of approximately 900 electrons/s and above a flux of approximately 2500 electrons/s. The average error on the observed flux is equal to 30.9 electrons/s and is therefore not visible in the lower figure.

Chapter 4

Data analysis methods

In this chapter we will discuss the computational methods used to analyse all quiescent intervals or quarters of the objects listed in table 3.1. The programming language Python is used to perform all methods. In section 4.1, we describe how we search for the rms-flux relation in a light curve. We then statistically determine whether there is a real correlation between rms variability and mean flux, and if so, whether the correlation is best described by a linear model. In section 4.2, we describe how the bootstrapping method is used to calculate the errors on the gradient and intercept of the fitted rms-flux relation.

4.1 Finding the rms-flux relation

To demonstrate how the rms-flux relation is recovered from a data set, we have used artificial light curves simulated according to the T&K algorithm (see chapter 2). By multiplying zero-centred Lorentzian-shaped noise time series with different break frequencies, the resulting light curve will display the rms-flux relation since all time scales are coupled. This is a very approximate model of an accretion disk, where the number of noise time series used corresponds to the number of annuli within the disc. We therefore use such an artificial light curve to design the method since we know that it must show a rms-flux relation. The light curve used in this section consists of the multiplication of ten zero-centred Lorentzian-shaped noise time series of which break frequencies ranging from 300 to 900 Hz.

In section 4.1.1, the initial calculations of the rms variability and mean flux will be done. The scatter of these results will be reduced and the resulting rms-flux relation will be fit in section 4.1.2. In section 4.1.3, we will statistically quantify the correlation between rms variability and mean flux and measure the goodness-of-fit of the linear model.

4.1.1 Initial calculation

The first step in the detection of the rms-flux relation consists of splitting the light curve into a certain number of bins. The number of flux measurements in each bin gives us the time scale at which we investigate flickering variability, since every measurement is taken at the short cadence sampling frequency. The number of bins is therefore calculated by dividing the number of data points through the desired time scale, given in multiples of the short cadence sampling frequency, which is equal to 58.8 s.

The artificial light curve $L(t)$ is split into B bins with each N measurements. For each of the B bins, we want to calculate the mean flux and the intrinsic variability of the flux measurements within the bin. The mean flux μ_1 and variance σ_1^2 of the measurements within each bin are given by:

$$\mu_1 = \frac{1}{N}\sum_{i=0}^{N} L(t_i),$$
$$\sigma_1^2 = \frac{1}{N-1}\sum_{i=0}^{N} \left(L(t_i) - \mu_1\right)^2 \ .$$

In order to obtain the intrinsic variance $\sigma_{1,intr}^2$ within each bin, we subtract the Poisson noise from the total variance:

$$\sigma_{1,intr}^2 = \sigma_1^2 - \mu_1,$$

since we have for Poisson noise that $\sigma^2 = \mu$. This step will not be performed when using simulated data as simulated time series do not include Poisson noise: the variance of the measurements within each bin is equal to its intrinsic variance. It will be performed when applying the method to *Kepler* data. The error on the intrinsic variance $\epsilon_{1,intr}$ within each bin is calculated by [2]:

$$\epsilon_{1,intr} = \sigma_{intr}^2 \sqrt{\frac{2}{N-1}} \ .$$

The intrinsic variance is subsequently converted to the rms variability of the bin by taking the square root:

$$\sigma_{1,rms} = \sqrt{\sigma_{1,intr}^2} \ .$$

The error on the rms variability is calculated by error propagation

$$\epsilon_{1,rms} = \frac{1}{2}\ \sigma_{1,rms}\ \frac{\epsilon_{1,intr}}{\sigma_{1,intr}^2} \ . \tag{4.1}$$

The first step in recovering the rms-flux relation is hence a binning over time of the light curve. The results of the first binning of the simulated time series are shown in figure 4.1. The time scale under investigation corresponds to approximately ten minutes. Even though the rms-flux data in figure 4.1 is scattered, especially at higher mean fluxes, a monotonically increasing trend is visible.

4.1.2 Reduction of scatter and fitting

The B bins, each with its mean flux and rms variability, are then sorted in order of ascending mean flux. This is done because the second binning, performed to reduce the scatter of the rms-flux data and increase the signal-to-noise ratio (SNR) per bin, is a binning over flux. In the second binning, the results are averaged out by rebinning the rms-flux data into ten bins. The number of original bins in each final bin is therefore equal to $B/10 = n$. The choice for ten final bins is made in accordance to Scaringi et al. (2012) [43]. It is made on an ad hoc basis without any statistical justification: a smaller or greater number of bins can be chosen, which will not significantly change the result.

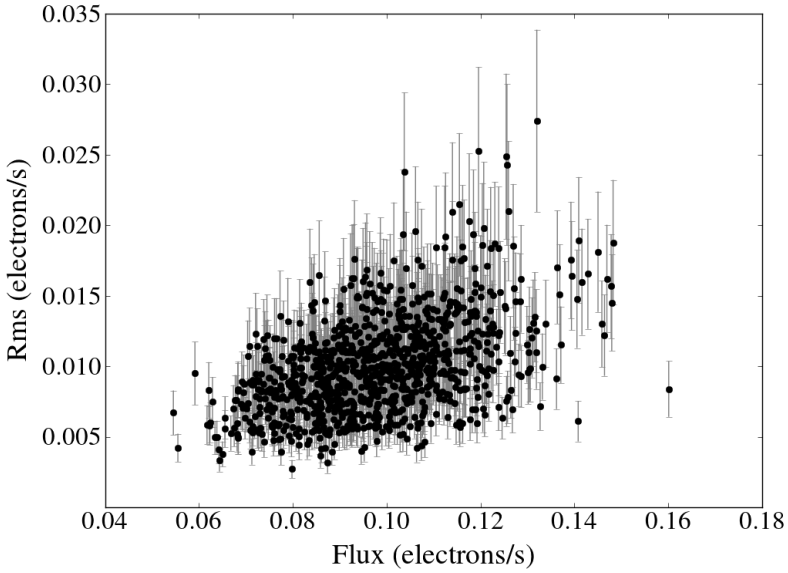

Figure 4.1: The rms-flux results after the first binning of the simulated data, consisting of the multiplication of ten zero-centred Lorentzian-shaped noise time series. The time scale under investigation corresponds to approximately 10 min.

We thus average the mean fluxes and intrinsic variabilities of the first binning results within each final bin. The mean flux and intrinsic variance of each of the ten final bins is calculated by

$$\mu_2 = \frac{1}{n}\sum_{j=0}^{n} \mu_1^j = \overline{\mu}_1,$$

$$\sigma^2_{2,intr} = \frac{1}{n}\sum_{j=0}^{n} \sigma^2_{(1,intr)j} = \overline{\sigma}^2_{1,intr} \ .$$

The error on the intrinsic variance $\sigma^2_{2,intr}$ is equal to the scatter of the intrinsic variances within each bin, divided through the square root of the number of data points n within each bin [2]:

$$\epsilon_{2,intr} = \sqrt{\frac{1}{n}\ \frac{\sum_{j=0}^{n}\left(\sigma^2_{(1,intr)j} - \overline{\sigma}^2_{1,intr}\right)^2}{n-1}} \ .$$

Again, the rms variability $\sigma_{2,rms}$ of each bin is calculated by taking the square root of its intrinsic variability. The error on the rms variability is calculated as in equation 4.1 by error propagation.

A linear model is fitted to the ten resulting rms-flux data points using a *linear regression* method of the IvS Python repository. The linear regression method fits a straight line to the data by minimising the sum of the squared residuals [24]. Applying the method to the ten rms-flux data points gives us the gradient and intercept of the fitted rms-flux relation, together with their errors. The errors given by the linear regression method will not be used when fitting the rms-flux relation in *Kepler* data. We will expand on bootstrapping in section 4.2, which will be used to calculate more accurate errors on the parameters of

the rms-flux relation.

Figure 4.2 shows the results of the final binning. Compared to the results of the first binning shown in figure 4.1, the scatter of the rms-flux points has clearly been reduced: a linear relation is now clearly visible. Using the linear regression method, a linear fit with a gradient of 0.104 ± 0.006 and an intercept of $(2 \pm 6) \times 10^{-6}$ is found. The errors quoted are those obtained from the linear regression method.

When the method is applied to *Kepler* data of a quiescent interval, we will first subtract the mean flux value of the entire quiescent interval from the light curve. This removes the correlation between gradient and intercept, which reduces the error on the fitted intercept significantly.

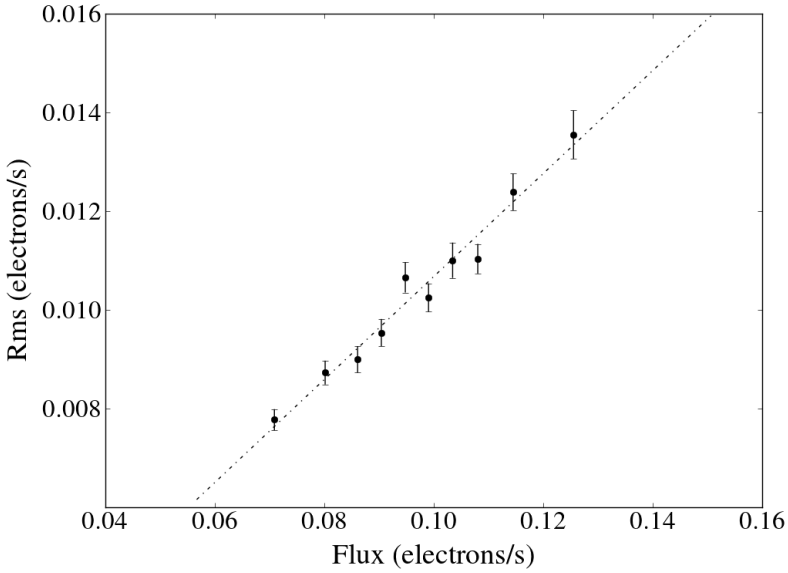

Figure 4.2: The rms-flux results after the second binning of the simulated data, consisting of the multiplication of three Lorentzian-shaped noise time series. The time scale under investigation corresponds to approximately 10 min. The relation found by linear regression has a gradient of 0.104 ± 0.006 and an intercept of $(2 \pm 6) \times 10^{-6}$.

4.1.3 Quantifying the relation and its linearity

We want to statistically quantify whether the rms variabilities and mean fluxes are indeed correlated, and if so, whether the underlying relation is linear. To determine the correlation between both data sets, we calculate the *Spearman's rank correlation coefficient* ρ. This is a non-parametric test that uses statistical ranks of the data rather than their actual values. These statistical ranks are obtained by putting the data in ascending order and assigning them their corresponding rank. The Spearman's rank correlation coefficient is given by

$$\rho = 1 - \frac{6 \sum_{i=0}^{N} d_i^2}{N(N^2 - 1)},$$

with d_i the difference in rank of corresponding variables and N the number of data, which is in our case equal to ten. The coefficient has values between -1 and 1, corresponding respectively to a positive or negative correlation, with 0 corresponding to no correlation at all [56]. The rms-flux relation would hence ideally result in $\rho = 1$.

We have made use of a Python SciPy method to calculate ρ. This method also calculates the p-value corresponding to ρ. This value indicates the probability that an uncorrelated system produces a data set with a Spearman's rank coefficient as extreme as the coefficient computed from the analysed data set. A coefficient close to one with a small p-value hence strongly indicates a positive correlation [26].

To determine if the correlation is best described by a linear model, we use the *reduced chi-squared* χ^2_{red} of the fitted model to determine the goodness-of-fit. This is calculated by

$$\chi^2_{red} = \frac{1}{K} \sum_i^N \left(\frac{\sigma^2_{2,rms} - y_i}{\epsilon_{2,rms}} \right)^2$$

with y_i the expected measurement given by the linear fit and K the degrees of freedom of the model. As there are ten data points and the linear fit has two parameters (gradient and intercept), we have that $K = 8$ [3].

When the model is correct and fits the data as expected, we should have $\chi^2_{red} \simeq 1$. The error on the prediction of $\chi^2_{red} = 1$ is given by $\sqrt{2/K}$: when an obtained χ^2_{red} value lies within $\Delta\chi^2_{red} = 1 \pm 0.5$, the fit can be considered as good. When $\chi^2_{red} < 1$, the model "overfits" the data by describing the errors on the data rather than the data itself. When $\chi^2_{red} > 1$, the model resulted in a "bad" fit to the data [3].

When calculating the reduced chi-squared of a linear fit to the rms-flux relation found in a light curve, it will most likely not be exactly equal to one because of the intrinsic scatter of the data. Whenever $\chi^2_{red} \lesssim 1$ or $\chi^2_{red} \gtrsim 1$, we need to take the visual evidence of a plot of the fitted rms-flux relation into account.

For the fit to the rms-flux data of the simulated data performed in this section, the Spearman's rank coefficient is equal to 0.99 with a p-value of 9.3×10^{-8}. Rms variability and mean flux are hence positively correlated. The reduced chi-squared of the linear fit is equal to 1.11. This lies within $\Delta\chi^2_{red} = 1.5$, and we can therefore state that the linear model provides a good fit to the rms-flux data: as expected, there is a linear rms-flux relation in the simulated data.

4.2 Error determination via bootstrapping

When fitting the rms-flux relation to a linear model by linear regression, we obtain the intercept and gradient of the relation together with the errors on these parameters. However, we will use a more reliable statistical method called *bootstrapping* for the determination of the errors on the fitted gradient and intercept.

In section 4.2.1, we will introduce the bootstrapping method and compare it to Monte Carlo methods. Bootstrapping is then applied to determine the errors of the gradient and intercept of the fitted rms-flux relation in section 4.2.2.

4.2.1 Bootstrapping and Monte Carlo methods

Bootstrapping is a non-parametric resampling method used to estimate the sampling distribution underlying a statistic of interest. As it is non-parametric, the distribution underlying the statistic of interest does not need to be known. The population from which the resampling is done is the original data set. Simplistically put, bootstrapping lets the data speak for itself since the method does not rely on any a priori assumptions on the distribution of the statistic of interest [10, 3].

Monte Carlo methods are resampling methods as well, but are parametric in nature: they require that the distribution of the statistic of interest is known. This is essential to the resampling process, as the Monte Carlo method does not resample the original data set but relies on the generation of artificial data. This has the practical implication that Monte Carlo methods are more time-consuming since they require more computations than bootstrapping methods [1].

When fitting the rms-flux relation, the statistics of interest are the gradient and intercept of the linear fit. The model describing their distributions is still subject to a lot of uncertainty [4, 39]. The bootstrapping method is hence more robust than Monte Carlo methods, and we have therefore chosen for the bootstrapping method for the error determination of the gradient and intercept of the fitted rms-flux relation.

4.2.2 Bootstrapping the rms-flux relation

As mentioned earlier, the statistics of interest of the fitted rms-flux relation are its gradient and intercept. We estimate the sampling distributions of these parameters by bootstrapping the light curve. The standard deviations of the sampling distributions are then adopted as the errors of the parameters.

A bootstrapped data set is produced by resampling the original light curve with replacement: a measurement is hence allowed to appear multiple times or not at all in the bootstrapped data set. We then determine and fit the rms-flux relation in the bootstrapped data set using the methods described in section 4.1. The resulting gradient a_{boot} and intercept b_{boot} are considered to be manifestations of their underlying sampling distribution. The light curve is bootstrapped 500 times in total: all 500 gradients and intercepts give us an estimate of the sampling distribution. The standard deviations of these distributions are then taken as the error on their respective parameters.

An illustration of the bootstrapping method can be seen in figure 4.3, which shows the distributions obtained for the gradient and intercept of the fitted rms-flux relation. The artificial light curve used is the same as in section 4.1. We will use the standard deviation of these distributions as errors on the gradient and intercept: for the simulated light curve of section 4.1, we hence find a linear rms-flux relation with a gradient of 0.10 ± 0.02 and an intercept of $(2 \pm 1) \times 10^{-6}$.

When working with *Kepler* data, we subtract the average flux value from the light curve. The bootstrapping method needs to be slightly modified in this case, as the mean flux value of the bootstrapped data set will most likely differ from that of the original data set. Subtracting a different mean flux value implies that the zero point in flux differs for each bootstrapped data set and the original light curve. This does not affect the gradient of the fitted rms-flux relation, but it does affect the intercept. We therefore need to make

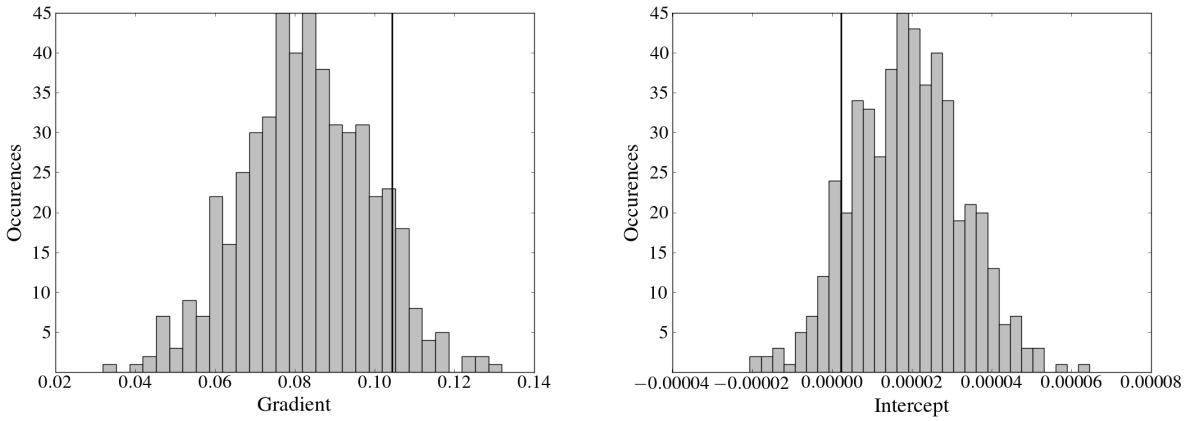

(a) Bootstrapped gradient a_{boot}
$\sigma = 0.02$

(b) Bootstrapped intercept b_{boot}
$\sigma = 1 \times 10^{-6}$

Figure 4.3: Distributions of the gradient and intercept of the rms-flux relation obtained through bootstrapping. The vertical line corresponds to the parameters found in the original data set. The light curve consists of the multiplication of ten zero-centred Lorentzian-shaped noise time series. The time scale under investigation corresponds to approximately 10 minutes.

a correction to the calculation of the intercept obtained from the bootstrapped data set, so that all intercepts are with respect to the same zero point in flux. The corrected intercept b_{corr} obtained from a bootstrapped data set is given by

$$b_{corr} = (\overline{L}_{orig} - \overline{L}_{boot}) \times a_{boot} + b_{fit} \tag{4.2}$$

with $\overline{L}_{orig}$ the mean of the original light curve, $\overline{L}_{boot}$ the mean of the bootstrapped light curve, and b_{fit} the intercept of the fitted rms-flux relation found in the original data set.

Chapter 5

Detection of the rms-flux relation

In this chapter, we will discuss the results of the analysis of all quiescent data of the objects listed in table 3.1. The rms-flux relation is detected in two of the eight CVs under consideration, namely V1504 Cyg and KIC 8751494. Section 5.1 will expand on and illustrate the detection. The other six CVs however do not show the rms-flux relation. This will be illustrated in section 5.2. We investigate why three quarters of the CVs under consideration do not have an observed rms-flux relation in section 5.3.

5.1 The rms-flux relation in V1504 Cyg and KIC 8751494

We have detected the rms-flux relation in the SU UMa star V1504 Cyg and the nova-like variable KIC 8751494. The relation is visible in every quiescent interval of V1504 Cyg, both separately and combined according to the quarter in which they are observed, and in all quiescent quarters of KIC 8751494. Moreover, the data has been analysed at multiple time scales and the rms-flux relation was found at every time scale.

In table 3.2, the number of data sets are listed: for KIC 8751494, we have 4 quarters, and for V1504 Cyg, we have 121 quiescent intervals which can be combined into 16 quarters. Because of the large amount of data sets, it is impossible to show all detected rms-flux relations. For both objects, we will therefore show the rms-flux relation found in one of their data sets at several time scales. The rms-flux relations shown are representative of those detected in all other data sets of the object at other sampled time scales.

In figure 5.1, we show the rms-flux relation detected in the combined quiescent intervals in Q4 of V1504 Cyg. The time scales shown correspond to 10, 40, 60, and 100 times the *Kepler* short cadence frequency. The Spearman's rank coefficients of the rms variabilities and mean fluxes are listed in the caption of each figure. For the four time scales, we have either $\rho = 1$ or $\rho \approx 1$ with very small p-values: we can state that there is a positive correlation between rms variability and mean flux. The goodness-of-fit of the linear model fitted to rms and flux is expressed by its reduced chi-squared, which is also listed in the caption. All fitted relations have a χ^2_{red} within $\Delta\chi^2_{red} = 1 \pm 0.5$: the linear model produces a good fit to the rms-flux data. Based on the values of ρ and χ^2_{red} for every time scale, we can state that we have detected the rms-flux relation at multiple time scales.

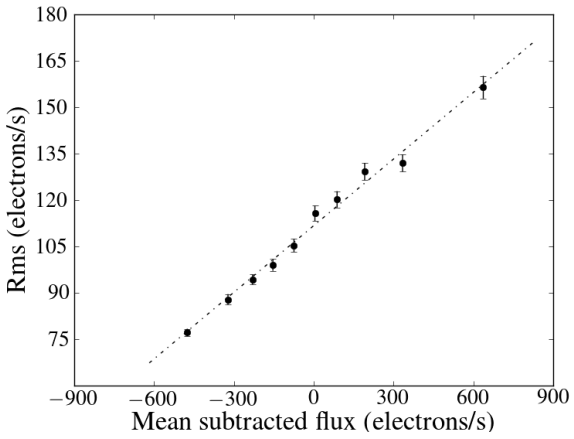

(a) Time scale ≈ 10 min
$a = 0.072 \pm 0.002$, $b = 111.7 \pm 0.1$
$\rho = 1$, p-value $= 0$ – $\chi^2_{red} = 1.02$

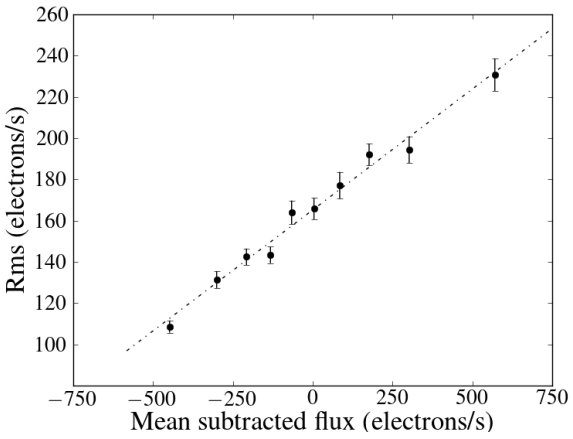

(b) Time scale ≈ 40 min
$a = 0.117 \pm 0.004$, $b = 165.2 \pm 0.2$
$\rho = 1$, p-value $= 0$ – $\chi^2_{red} = 1.05$

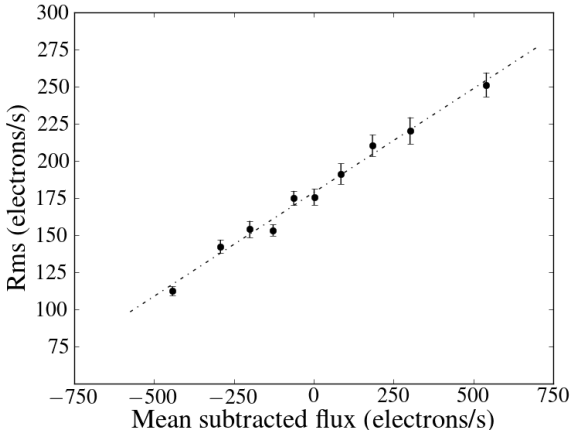

(c) Time scale ≈ 60 min
$a = 0.140 \pm 0.005$, $b = 178.7 \pm 0.2$
$\rho = 0.99$, p-value $= 9.3 \times 10^{-8}$ – $\chi^2_{red} = 1.23$

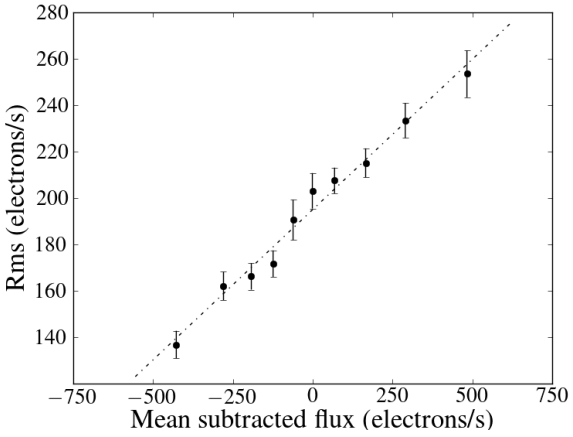

(d) Time scale ≈ 100 min
$a = 0.130 \pm 0.006$, $b = 195.0 \pm 0.2$
$\rho = 1$, p-value $= 0$ – $\chi^2_{red} = 0.57$

Figure 5.1: The rms-flux relation detected in the combined quiescent intervals of Q1 of V1504 Cyg for four different time scales. A mean flux value of 1628.7 electrons/s has been subtracted from the data set. The Spearman's rank coefficient ρ is given along with its p-value. The gradient a and intercept b of the linear fit are given as well, together with its reduced chi-squared value χ^2_{red}.

Figure 5.2a displays the reduced chi-squared distribution obtained after fitting the rms-flux relation in all quiescent intervals of V1504 Cyg The time scale under investigation corresponds to approximately 10 minutes. From the distribution, it is clear that the linear model is a good fit to the rms-flux data of most quiescent intervals. However, in some quiescent intervals, the fit resulted in $\chi^2_{red} \gg 1$. This is because the orbital period is clearly visible during those quiescent intervals, which gives the general shape of their light curves a sinusoidal trend. The presence of this trend affects the flux distribution, and hence the rms-flux relation. We will expand on the periods characteristic to V1504 Cyg and all other CVs in the appendix.

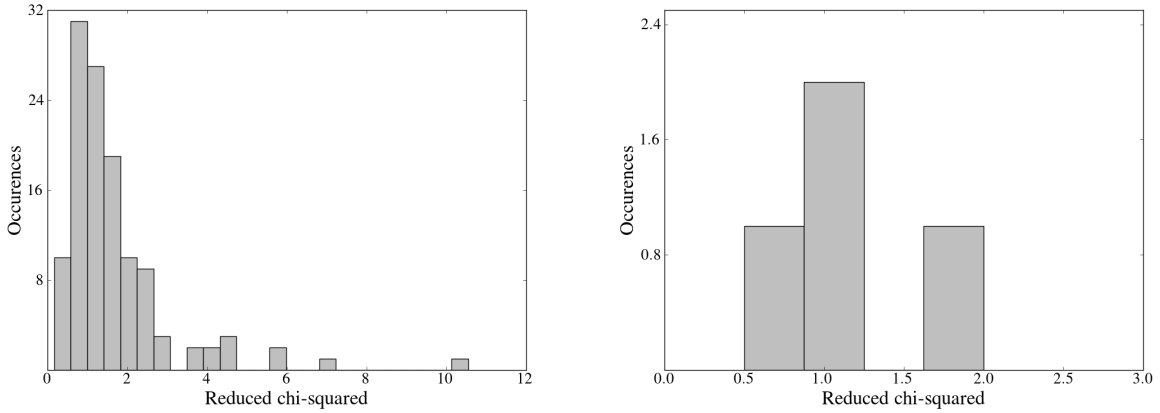

(a) V1504 Cyg (b) KIC 8751494

Figure 5.2: Reduced chi-squared distribution obtained after fitting the rms-flux relation detected in all quiescent intervals of V1504 Cyg and all quiescent quarters of KIC 8751494. The time scale under investigation corresponds to approximately 10 minutes.

In figure 5.3, we show the rms-flux relation detected in the quiescent quarter Q16 of KIC 8751494. The time scales sampled are the same as before, and correspond to approximately 10, 40, 60, and 100 minutes. The Spearman's rank coefficient and its corresponding p-value of the rms-variabilities and mean fluxes are again listed in each caption. They enable us to state that there is indeed a correlation between rms and flux at every time scale. The χ^2_{red} of the linear models fitted to rms and flux at every time scale are within $\Delta\chi^2_{red} = 1 \pm 0.5$. Based on the values of ρ and χ^2_{red} for every time scale, we can state that we have detected the rms-flux relation at multiple time scales.

The reduced chi-squared values obtained after fitting the rms-flux relation detected in all quiescent quarters of KIC 8751494 is shown in figure 5.2b. The time scale under investigation corresponds to approximately 10 minutes. Due to the smaller number of data sets, we cannot consider this figure to be a distribution. However, all χ^2_{red} values correspond to a good fit of the linear model to the rms-flux data.

From figures 5.1 and 5.3, we see that the gradient and intercept of the fitted rms-flux relation vary with time scale at which the data set is sampled in both objects. The variation of gradient and intercept with time scale will be discussed in chapter 6.

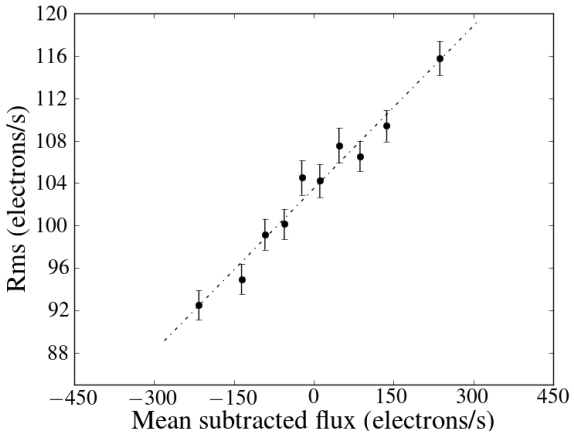

(a) Time scale ≈ 10 min
$a = 0.051 \pm 0.003$, $b = 103.48 \pm 0.03$
$\rho = 0.98$, p-value $= 1.5 \times 10^{-6}$– $\chi^2_{red} = 0.71$

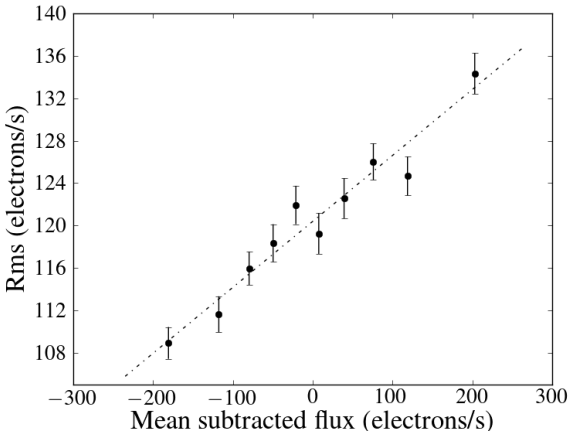

(b) Time scale ≈ 40 min
$a = 0.062 \pm 0.003$, $b = 120.3 \pm 0.03$
$\rho = 0.98$, p-value $= 1.5 \times 10^{-6}$ – $\chi^2_{red} = 1.00$

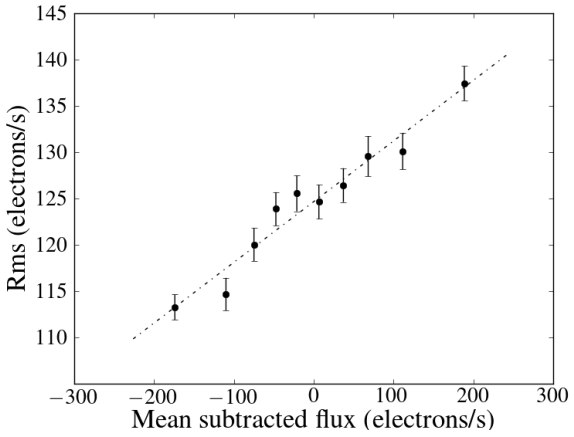

(c) Time scale ≈ 60 min
$a = 0.066 \pm 0.004$, $b = 124.66 \pm 0.03$
$\rho = 0.99$, p-value $= 9.3 \times 10^{-8}$–$\chi^2_{red} = 0.85$

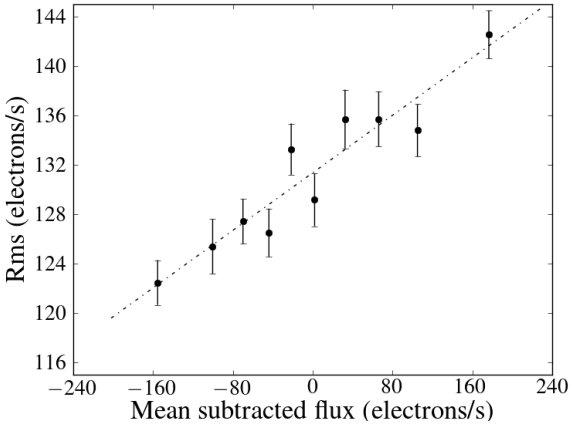

(d) Time scale ≈ 100 min
$a = 0.058 \pm 0.005$, $a = 131.35 \pm 0.03$
$\rho = 0.94$, p-value $= 5.5 \times 10^{-5}$–$\chi^2_{red} = 0.98$

Figure 5.3: The rms-flux relation detected in quiescent quarter Q16 of KIC 8751494 for four different time scales. A mean flux value of 3368.9 electrons/s has been subtracted from the data set. The Spearman's rank coefficient ρ is given along with its p-value. The gradient a and intercept b of the linear fit are given as well, together with its reduced chi-squared value χ^2_{red}.

5.2 The rms-flux relation in the other CVs

We would expect all eight CVs in table 3.1 to show the rms-flux relation. However, all data sets of the other six CVs were analysed in the same way as V1504 Cyg and KIC 8751494, but do not show the rms-flux relation on any sampled time scale. The total data set is too large to illustrate this for every quiescent interval of every object. We have selected the combined quiescent intervals in Q6 of the dwarf nova BOKS 45906 for illustration. The results from the analysis of this data set are representative for those from all other data sets in the other objects.

Figure 5.4 shows the results of the analysis of the combined quiescent intervals in Q6 of the dwarf nova BOKS 45906, sampled at time scales corresponding to approximately 10 and 60 minutes. For both time scales, the Spearman's rank coefficient of the rms variabilities and the mean fluxes imply that there is no correlation between them. The rms-flux relation is hence not present. These results are representative of those obtained at other time scales in all quiescent intervals of the six CVs in which the rms-flux relation is not detected.

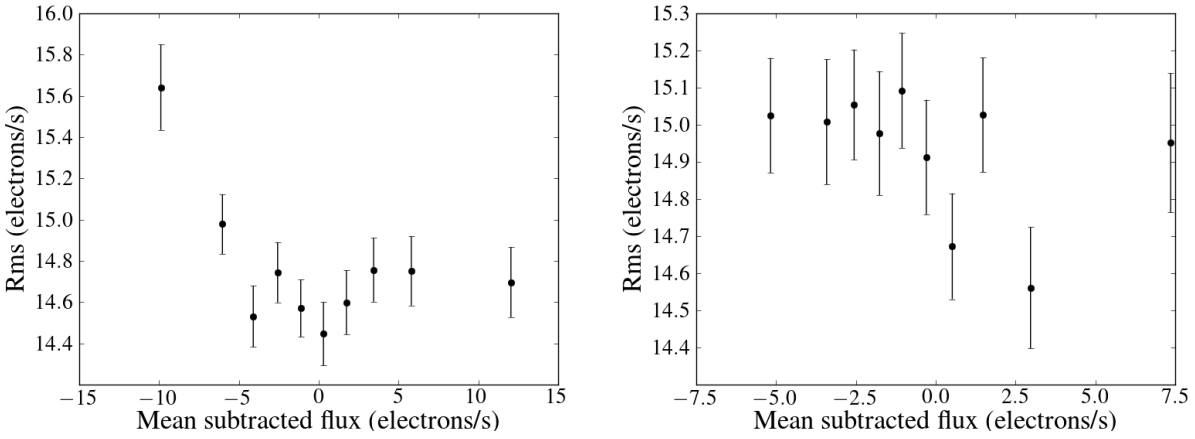

(a) Time scale ≈ 10 min
$\rho = -0.22$, p-value = 0.53

(b) Time scale ≈ 60 min
$\rho = -0.05$, p-value = 0.14

Figure 5.4: Results of the analysis of Q6 of BOKS 45906 at time scales of approximately 10 min and 60 min. A mean flux value of 80.3 electrons/s has been subtracted from the data. The Spearman's rank coefficient ρ is given along with its p-value.

5.3 Conditions for detection of the rms-flux relation

Out of the eight CVs listed in table 3.1, we have only detected the rms-flux relation in V1504 Cyg and KIC 8751494. We would expect all CVs under consideration to show the rms-flux relation, since flickering is thought to be a property of the quiescent intervals in CVs and the rms-flux relation is inherent to flickering. Not detecting the rms-flux relation can point towards the CV not showing any intrinsic flickering, but it is also possible that the quality of the data does not allow us to detect any intrinsic flickering.

Since CVs are thought to always show flickering, it is important that we determine why the rms-flux relation is not detected in three quarters of the CVs under consideration.

This will be done in three different ways, each complementing the others. In section 5.3.1, we will determine whether the light curves are dominated by instrumental noise. In section 5.3.2, we will compare the Poisson noise level of a light curve to its observed variability in order to determine whether any intrinsic variability is present in the light curve. The question will be approached in a more visual way in section 5.3.3, where we will compare PSDs of all objects.

5.3.1 Intrumental noise

In order to determine whether a light curve is dominated by instrumental noise, we fit the light curve with a linear model. When the reduced chi-squared of the fit is approximately equal to one, the data and its errors are accurately represented by the linear model. This implies that the variability visible in the light curve can be described by Gaussian distributed white noise [3]. In this case, the rms-flux relation cannot be detected as no intrinsic variability is visible in the light curve.

A linear model is fit to every quiescent interval or quarter of every object. We then average over all χ^2_{red} obtained from one object, so that each object is characterised by a single χ^2_{red}. The results are listed in table 5.1. We find that the average χ^2_{red} for the CVs with a detected rms-flux relation are much larger than one: the variability in the quiescent intervals or quarter is not due to white noise, but is intrinsic to the object.

For most CVs without a detected rms-flux relation, the average χ^2_{red} is approximately equal to one: the observed data and its errors of the quiescent intervals or quarters can be described by white noise. The CVs V334 Lyr and V363 Lyr have values of χ^2_{red} larger than one. The discrepancy of their χ^2_{red} is due to the orbital period of these systems being clearly visible during some of their quiescent intervals. As mentioned earlier, the sinusoidal trend that is present in the data affects the flux distribution and hence the rms-flux relation. From the results in table 5.1, we conclude that the rms-flux relation is only detected in CVs of which the light curves cannot be described by white noise.

Object	Average χ^2_{red}
BOKS 45906	1.06
V344 Lyr	3.21
V363 Lyr	7.66
V447 Lyr	1.15
V516 Lyr	1.35
V585 Lyr	1.31
V1504 Cyg	229
KIC 8751494	148

Table 5.1: Average χ^2_{red} of a linear fit to the quiescent intervals or quiescent quarters of all objects under consideration. CVs in which the rms-flux relation is detected are listed at the bottom.

5.3.2 Comparison of rms-variability to Poisson noise

Another way of determining whether any flickering variability is present in a light curve is by comparing its observed rms variability to its Poisson noise level. Flickering cannot be detected in a quiescent interval or quarter when its Poisson noise is larger than its rms variability, as the instrumental errors "overpower" the intrinsic variability in that case. We therefore calculate the Poisson noise, given by the square root of the average flux, of every quiescent interval or quarter together with its rms variability. The results of all quiescent intervals of an object are then averaged over, so that each object is characterised by a single value for average flux, Poisson noise, and rms variability. Note that averaging over several quarters will result in errors on these values, as the average flux observed of an object varies depends on the quarter. We will not calculate these errors, but will keep them in mind when comparing the objects.

In table 5.2, the average values of flux, Poisson noise, and observed rms variability are listed together with the fraction of Poisson noise to observed rms variability for every CV under consideration. It is clear that the average fluxes of V1504 Cyg and KIC 8751494 are at least an order of magnitude larger than those of all the other objects. Although this increases the level of Poisson noise for these objects, it also implies that the statistical errors on the measurements are smaller as more photons are detected. Whether the Poisson noise within a data set can hide any intrinsic scatter the object might show, is measured by the fraction of average Poisson noise level to average rms. When the fraction is approximately equal to one, the rms-flux relation cannot be detected as we cannot distinguish between Poisson noise and intrinsic variability from the object. These fractions are smaller than one for all CVs: the variability observed in all objects hence cannot be explained by Poisson noise only. Note that this analysis does not isolate the frequency range over which Poisson noise dominates any intrinsic variability in the light curve. In the next section, this frequency range will be visually determined by analysing its PSD.

The fractions for V1504 Cyg and KIC 8751494 are smaller than those of the other CVs by at least a factor of two. A larger fraction of the variability observed in these CVs is therefore due to intrinsic variability. We conclude that the rms-flux relation cannot be detected in the quiescent intervals or quarters of CVs of which the Poisson noise level is a large fraction of the rms variability of the measured data.

Object	Mean flux (electrons/s)	Mean Poisson noise (electrons/s)	Mean rms variability (electrons/s)	Poisson/rms
BOKS 45906	81.6	9.02	14.8	0.61
V344 Lyr	391	19.5	31.0	0.66
V363 Lyr	404	20.1	31.7	0.63
V447 Lyr	31.6	5.61	11.4	0.50
V516 Lyr	55.6	7.26	12.0	0.61
V585 Lyr	235	15.3	22.5	0.71
V1504 Cyg	1.90×10^3	43.5	299.9	0.15
KIC 8751494	3.81×10^3	61.7	174.9	0.35

Table 5.2: Mean flux level, rms variability and Poisson noise of all quiescent intervals, and the ratio of the average Poisson noise detected in all quiescent intervals and their average rms variability. The CVs with a detected rms-flux relation are listed at the bottom.

5.3.3 Visual analysis of the PSD

The PSD of a light curve is a visual way to determine whether an object shows intrinsic flickering variability or is overpowered by Poisson noise. If flickering variability is present, the PSD has the shape of zero-centred Lorentzian noise (figures 2.3b and 2.4b). Up to the break frequency, which is related to the viscous frequencies within the accretion disc, the object displays flickering variability. For frequencies above the break frequency, the variability falls off. Note that when plotting the PSDs as power × frequency, flickering variability has a flat shape in the PSD. If a light curve is overpowered by Poisson noise, this is clearly visible in its PSD. A simulation can be seen in figure 2.1b. When plotting the PSDs as power × frequency, Poisson noise increases with frequency in the PSD.

For each object, we calculate the PSD of each data set available. It is infeasible to show all obtained PSDs. We illustrate the results of each object with one PSD, representative of all other PSDs for that object. The results are shown in figures 5.5 and 5.6, together with the frequency corresponding to the longest time scale at which the rms-flux relation has been analysed, approximately 140 minutes. We have hence only searched for the rms-flux relation at frequencies above this frequency.

Figure 5.5 shows PSDs for V1504 Cyg and KIC 8751494. Intrinsic flickering variability is clearly visible in both objects, as is expected since these systems show the rms-flux relation. The break frequency is different for both objects, which might point towards differences in the accretion discs of these two systems. This is possibly due to the fact that V1504 Cyg is a SU UMa dwarf nova and KIC 8751494 a nova-like variable. A peak and its harmonics are visible in the PSD of KIC 8751494. We will determine the period corresponding to these peaks in the appendix.

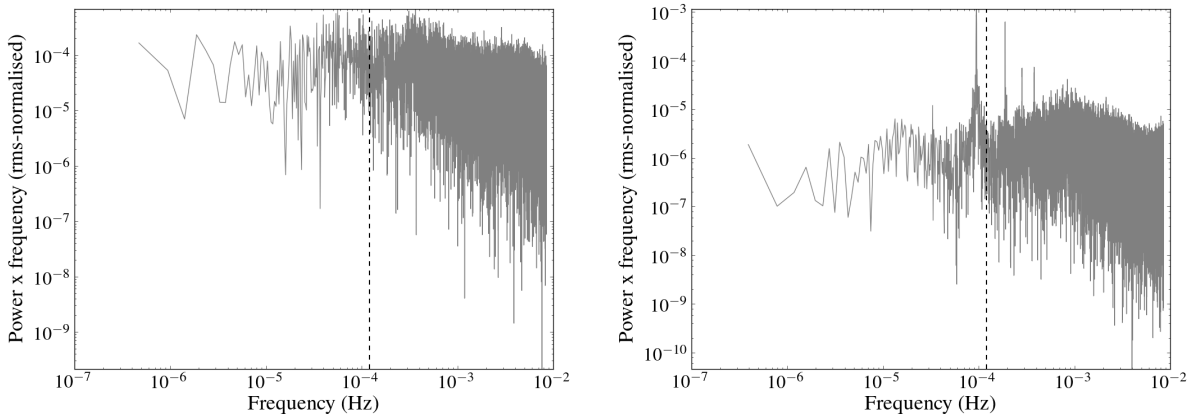

(a) V1504 Cyg
PSD of combined quiescent intervals of Q2

(b) KIC 8751494
PSD of quiescent quarter Q3

Figure 5.5: Representative PSDs of the CVs with a detected rms-flux relation. The rms-flux relation is calculated for frequencies above the marked frequency, which corresponds to a time scale of approximately 140 minutes.

Figure 5.6 shows PSDs for the six CVs in which the rms-flux relation was not detected. The light curves under investigation are clearly dominated by Poisson noise. The rms-flux relation can therefore not be determined in these objects. Peaks are visible in the PSDs of BOKS 45906 and V447 Lyr. These peaks correspond to periods characteristic to these

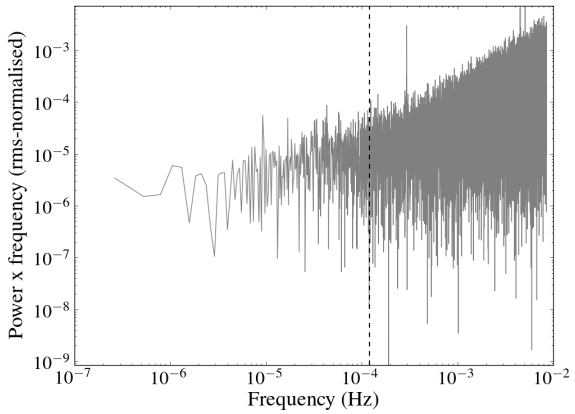

(a) BOKS 45906
PSD of combined quiescent intervals of Q6

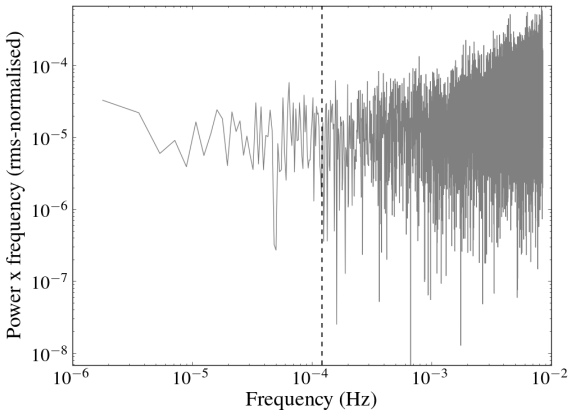

(b) V344 Lyr
PSD of combined quiescent intervals of Q7

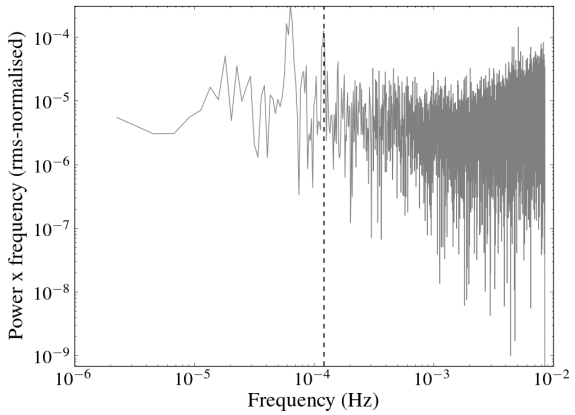

(c) V366 Lyr
PSD of quiescent quarter Q16

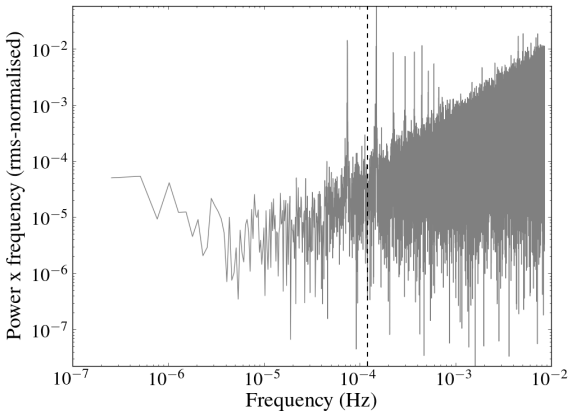

(d) V447 Lyr
PSD of quiescent quarter Q13

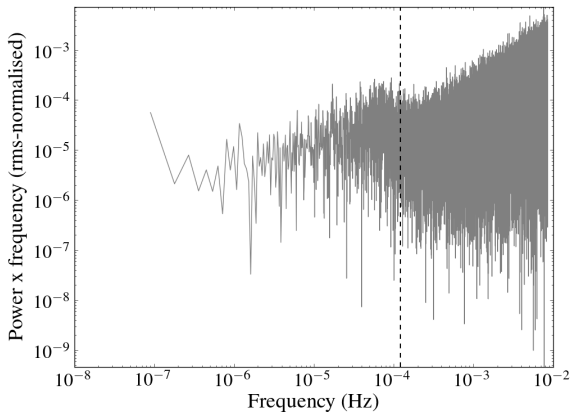

(e) V516 Lyr
PSD of quiescent quarter Q9

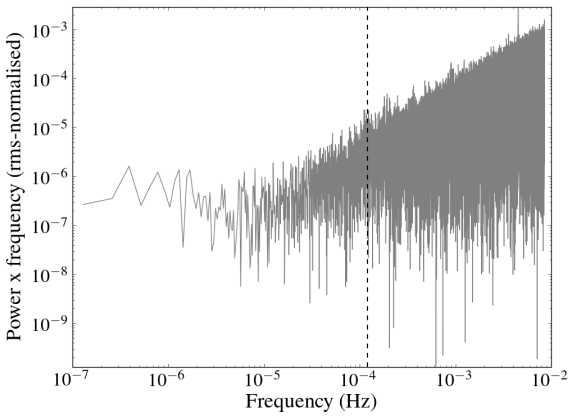

(f) V585 Lyr
PSD of quiescent quarter Q14

Figure 5.6: Representative PSDs of the CVs without a detected rms-flux relation. The rms-flux relation is calculated for frequencies above the marked frequency, which corresponds to a time scale of approximately 140 minutes.

systems, and will be discussed in the appendix. At high frequencies, peaks are clearly visible in the PSDs of BOKS 45906, V363 Lyr, V447 Lyr, and V585 Lyr. These peaks moreover occur at the same frequencies. They are caused by an artefact in the data, and correspond to the inverse of the long cadence sampling period and its harmonics [17].

The previous method of comparing the Poisson noise level to the measured rms variability tells us which fraction of the observed variability is due to Poisson noise. However, it does not constrain the range of frequencies over which the Poisson noise overpowers any intrinsic variability. It is clear that for the six CVs without a detected rms-flux relation, the power in the sampled frequency range is dominated by Poissonian noise.

Taking the results of all previously discussed methods into account, we can conclude that the rms-flux relation has been detected in the objects for which the data allowed for its detection. Only the quiescent intervals and quarters of V1504 Cyg and KIC 8751494 display flickering variability, enabling us to detect the rms-flux relation in these systems. The quiescent intervals and quarters of all other CVs are dominated by Poisson noise, making it impossible detect the rms-flux relation in these systems. The rms-flux relation is therefore not *not* detected in these systems.

Chapter 6

Discussion

When analysing the rms-flux relation of V1504 Cyg and KIC 8751494, we found that the gradient and intercept of the linear fit vary with the time scale sampled during the analysis. This can be seen in figures 5.1 and 5.3. Parameters found at a specific time scale also vary with the data set analysed; in other words, the parameters vary with time. The variation of the parameters of the linear fit with time scale will be discussed in section 6.1. Their variation with time will be discussed in section 6.2.

The detection of the rms-flux relation is only one of the properties of flickering which points towards the coupling of the short and long time scales within the accretion disc. This coupling is also indicated by a lognormal flux distribution. We will briefly discuss the flux distribution of the CVs under investigation in section 6.3.

6.1 Variation of the parameters of the fitted rms-flux relation with time scale

When the rms-flux relation of a quiescent interval or quarter is sampled at several time scales, the gradient and intercept of the linear fit to the rms-flux relation vary with the time scale under consideration. This is observed in both V1504 Cyg and KIC 8751494. The variations however depend on the object. We will illustrate these variations in V1504 Cyg by analysing the combined quiescent intervals of Q4 and in KIC 8751494 by analysing the quiescent quarter Q2. The variations found in these data sets are representative of those found in all other data sets for both objects.

In figure 6.1, the variation of the intercept of the fitted rms-flux relation with the time scale sampled is shown for V1504 Cyg and KIC 8751494. The time scales sampled range from approximately 5 to 140 minutes. It is clear that the intercept increases with time scale in both CVs. At longer time scales, the increase appears to flatten. At shorter time scales, the increase steepens.

The intercept of the rms-flux relation is a measure of the constant variability power observed, as it corresponds to the rms variability at zero flux. The flattening observed in figure 6.1 hence corresponds to the PSD flattening at frequencies below the local viscous frequencies within the disc. At frequencies below this "kink", the total variability observed does not increase any more with decreasing frequency, equivalent to increasing time scale. This is illustrated in figure 6.2, which shows the PSD corresponding to the

data sets analysed in figure 6.1. Time scales corresponding to approximately 30 and 100 minutes are plotted onto the PSDs. At shorter time scales, the number of flux measurements in each bin after the first binning is smaller. The measured variability within each bin is then smaller, while the level of Poisson noise is the same at all time scales. Subtracting the Poisson noise from the measured variability in order to obtain the intrinsic variability therefore has a larger influence at the shortest time scales, which explains the steep increase of the intercept.

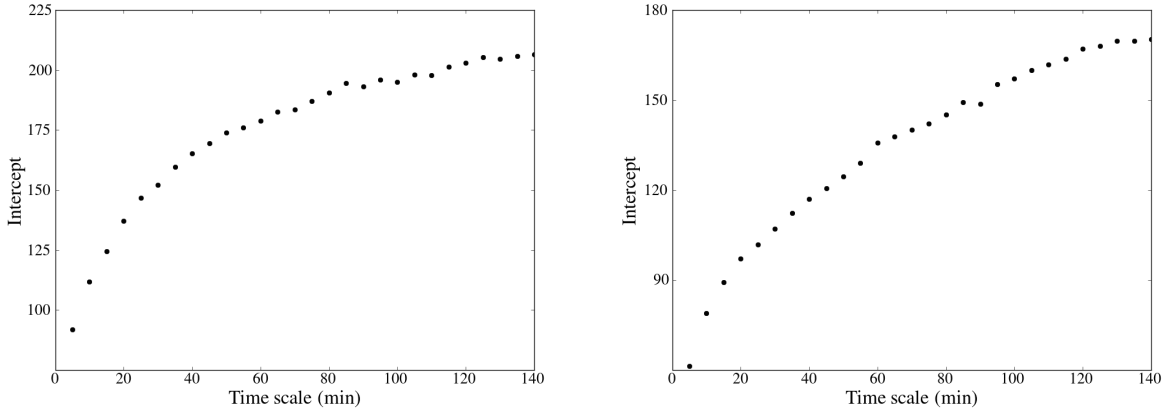

(a) V1504 Cyg
Combined quiescent intervals of Q4

(b) KIC 8751494
Quiescent quarter Q2

Figure 6.1: Variation of the intercept of the fitted rms-flux relation with time scale in V1504 Cyg and KIC 8751494. The errors on the intercept are too small to be visible. For V1504 Cyg, the average error is 0.2 electrons/s. For KIC 8751494, the average error is 0.08 electrons/s.

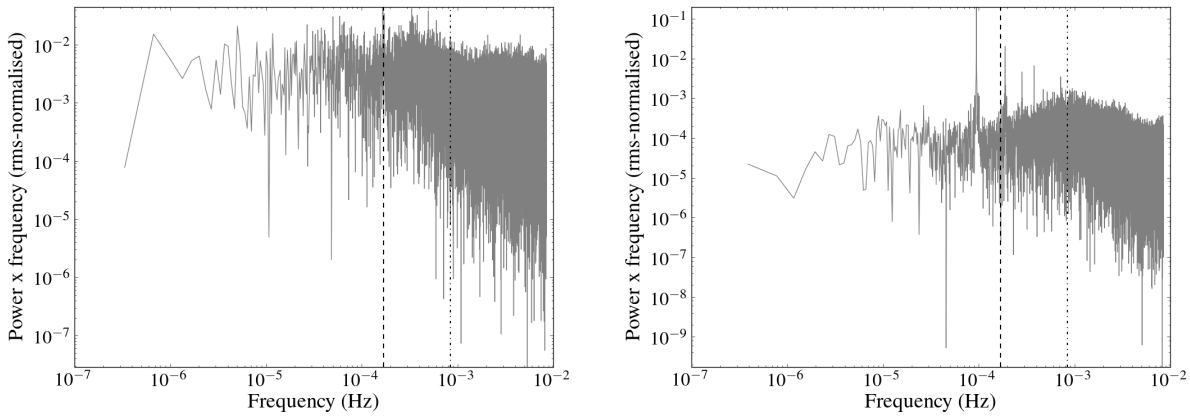

(a) V1504 Cyg
PSD of combined quiescent intervals of Q4

(b) KIC 8751494
PSD of quiescent quarter Q2

Figure 6.2: Representative PSDs of V1504 Cyg and KIC 8751494. The striped-dotted lines correspond to a time scale of approximately 30 minutes. The striped lines correspond to a time scale of approximately 100 minutes.

In figure 6.3, the variation of the gradient of the fitted rms-flux relation with the time scale sampled is shown for V1504 Cyg and KIC 8751494. The time scales sampled range from approximately 5 to 140 minutes. The variation observed depends on the object: in V1504 Cyg, the gradient increases with increasing time scale, while in KIC 8751494 the gradient decreases with time scale until approximately 80 minutes, after which it increases.

The gradient of the rms-flux relation is a measure of how fast the total variability power increases with increasing flux. This cannot be explained as straightforwardly as the variation of the intercept, as the PSD does not provide us with information on how fast the total variability power increases. Moreover, as the variation is different for both objects, this might point towards different properties of their respective accretion discs. Again, this is possibly due to the fact that V1504 Cyg is a SU UMa dwarf nova and KIC 8751494 a nova-like variable. Further research is required to explain the variation of the gradient of the fitted rms-flux relation with time scale.

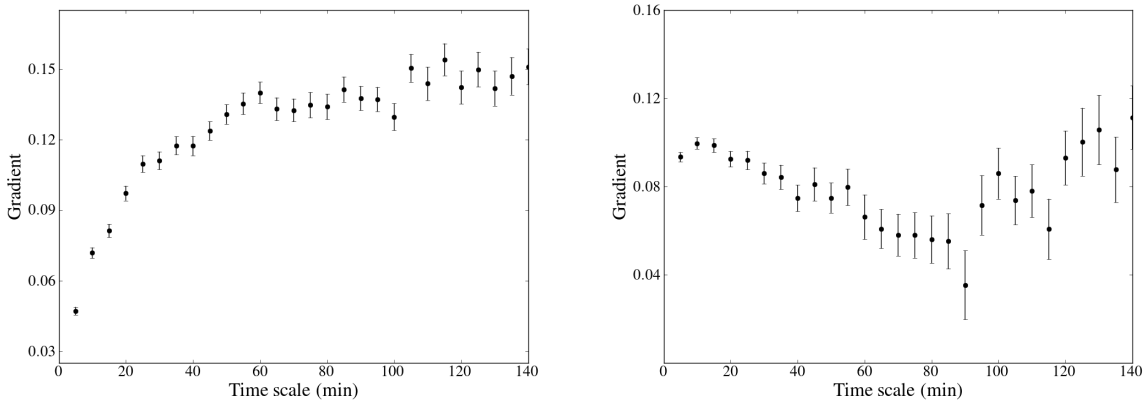

(a) V1504 Cyg
Combined quiescent intervals of Q4

(b) KIC 8751494
Quiescent quarter Q2

Figure 6.3: Variation of the gradient of the fitted rms-flux relation with time scale in V1504 Cyg and KIC 8751494.

6.2 Variation of the parameters of the fitted rms-flux relation with time

When determining the rms-flux relation at a single time scale in all quiescent data sets of V1504 Cyg and KIC 8751494, the gradient and intercept of the fitted relation vary with the data set under consideration. As every data set is observed at a different time, the parameters of the fitted relation vary with time. Since there are only four data sets available for KIC 8751494, it is difficult to determine whether the gradient and intercept actually vary with time. V1504 Cyg has 121 quiescent intervals, which can be combined into 16 quarters. With this amount of data sets, any variation of gradient and intercept with time will be clearly visible.

Figure 6.4 shows the variation of the gradient of fitted the rms-flux relation with time in V1504 Cyg. The time scale sampled corresponds to approximately 10 minutes. The gradients of the rms-flux relation found in the quiescent intervals combined into quarters

and in the quiescent intervals separately are both shown in the figure. Between 2455200 and 2455600 JD, about one year, the gradient of the rms-flux relation appears to decrease with time. This might be due to changes within the accretion disc, but further research is needed. Before and after this period, the measured gradients appear scattered.

Figure 6.5 shows the variation of the intercept of the fitted rms-flux relation with time in V1504 Cyg. The time scale sampled corresponds to approximately 10 minutes. The intercepts of the rms-flux relation found in both the quiescent intervals separately and combined into quarters are both shown in the figure. There appears to be a downward trend, but the data is scattered. Further research is needed in order to quantify any present variations of gradient and intercept with time and determine their origin.

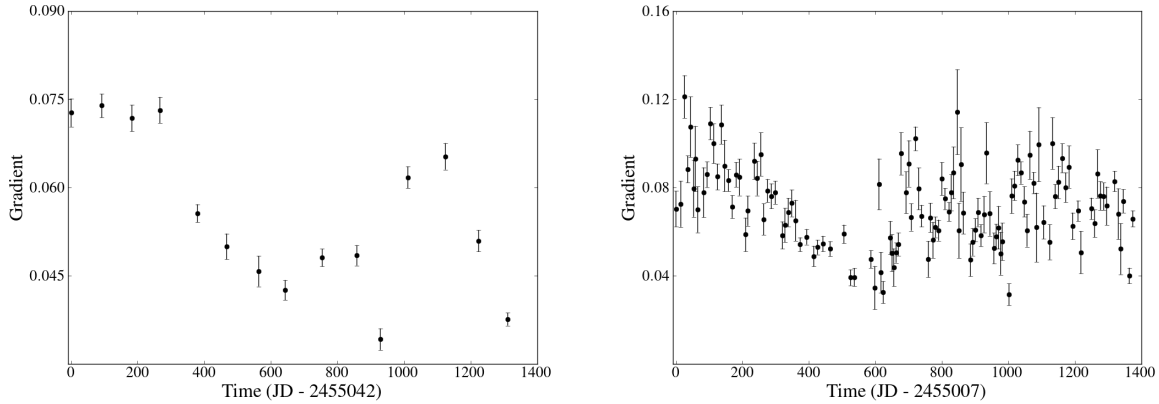

(a) Quiescent intervals combined into quarters (b) Quiescent intervals separately

Figure 6.4: Variation of the gradient of the fitted rms-flux relation with time in V1504 Cyg. The time scale sampled is approximately 10 minutes.

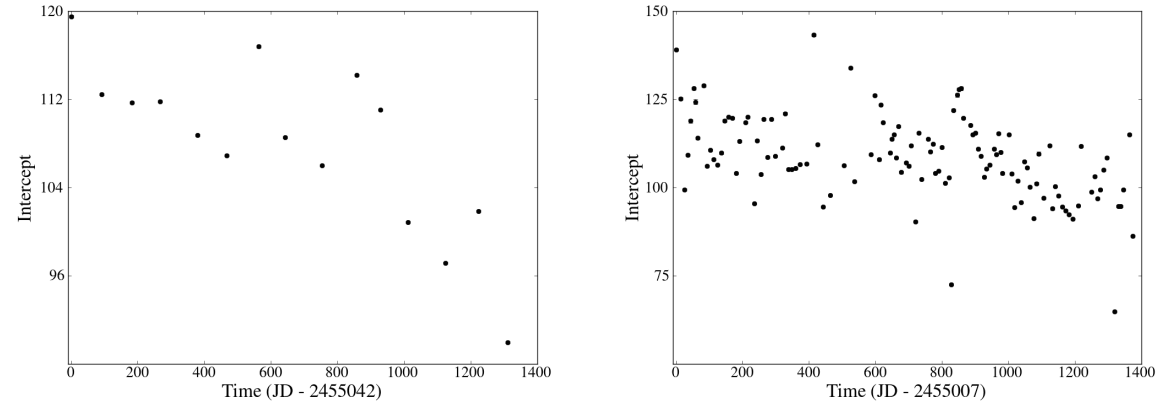

(a) Quiescent intervals combined into quarters (b) Quiescent intervals separately

Figure 6.5: Variation of the intercept of the fitted rms-flux relation with time in V1504 Cyg. The time scale sampled is approximately 10 minutes. The errors on the intercept are too small to be visible. For the quiescent intervals combined into quarters, the average error is 0.09 electrons/s. For the quiescent intervals separately, the average error is 0.3 electrons/s.

6.3 Flux distribution of V1504 Cyg and KIC 8751494

According to the fluctuating accretion model, objects with a detected rms-flux relation also have a lognormal flux distribution. The rms-flux relation indicates that the short and long time scales of flickering within the accretion disc are coupled. In the fluctuating accretion model, this is achieved by multiplying all variations. The multiplicative coupling naturally produces a lognormal flux distribution.

Figure 6.6 shows the normalised flux distribution for the combined quiescent intervals of Q5 of V1504 Cyg and the quiescent quarter Q2 of KIC 8751494. The flux is normalised by dividing the measured flux through the average measured flux value. These distributions are representative for the flux distributions found in all other data sets. It is clear that both objects display a lognormal flux distribution, especially in the distribution of V1504 Cyg. This enforces the fluctuating accretion model. However, the distribution needs to be fit in order to obtain the goodness-of-fit of a lognormal distribution.

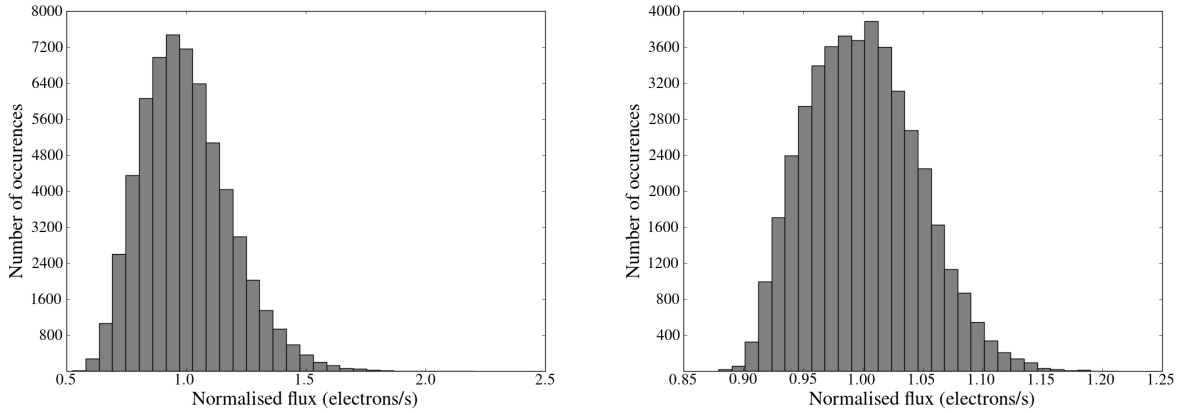

(a) V1504 Cyg (b) KIC 8751494

Figure 6.6: Normalised flux distribution of V1504 Cyg and KIC 8751494. For V1504 Cyg, the combined quiescent intervals of Q5 are analysed. For KIC 8751494, the quiescent quarter Q2 is analysed.

Chapter 7

Conclusion

In this master's thesis, we have probed the flickering variability of eight CVs in the *Kepler* field-of-view. CVs are not the only systems that display flickering variability. Other compact interacting binaries, such as XRBs and AGN, also display this type of aperiodic broadband variability. Flickering variability is accretion-induced and originates in the accretion disc surrounding the central object. Other types of accretion-induced variability have also been observed in CVs, XRBs, and AGN. These shared properties lead to the hypothesis that the physics governing accretion discs is independent of mass, size or type of the central compact object. In other words, the nature of accretion is thought to be universal.

Because of the availability of high quality X-ray light curves, mainly thanks to the NASA *Rossi X-ray Timing Explorer* mission, flickering variability has been studied in more detail in XRBs and AGN. The rms-flux relation is one of the properties of flickering variability. It is a linear relation between the rms amplitude of the variability of a light curve and its mean flux. The rms-flux relation has been detected in multiple XRBs and AGN. For the analysis of flickering variability in CVs, long uninterrupted light curves at optical wavelengths are needed. Since the launch of the *Kepler* satellite, large amounts of high-quality data suitable for its analysis in CVs became available. Nevertheless, only one CV has an observed rms-flux relation: MV Lyr, which is in the *Kepler* field-of-view. The aim of this thesis is to detect the rms-flux relation in as many CVs in the *Kepler* field-of-view as possible.

We have found eight CVs in the *Kepler* field-of-view for which short cadence data are available, excluding MV Lyr. Since we want to analyse flickering variability, any outbursts and eruptions need to be neglected. These cataclysmic events dominate the light curve, making it difficult to detect flickering variability. Also, they influence the flux distribution and hence the rms-flux relation. For all eight CVs, the quiescent intervals have been selected using a conservative range, making sure that the system is fully in its quiescent state. These quiescent intervals have also been combined according to the *Kepler* quarter in which they were observed. Not all CVs displayed outbursts, for these systems the light curve has been split into quiescent quarters.

The rms-flux relation is detected in two CVs: V1504 Cyg and KIC 8751494. Moreover, we have detected the rms-flux relation in every quiescent data set of both objects. The rms-flux relation could not be detected in the other six CVs. This might point towards these CVs not displaying any flickering variability, which would not be expected. All data

sets have been analysed and we found that the rms-flux relation is not detected in light curves in which instrumental noise overpowers any intrinsic variability of the object. The rms-flux relation is hence not *not* detected in those six CVs.

When analysing the rms-flux relation in V1504 Cyg and KIC 8751494, we found that the gradient and intercept of the fitted rms-flux relation of a quiescent data set vary with the time scale sampled. The variation of the intercept is mainly caused by the PSD shape of the data set, as the intercept is a measure of the constant variability power observed. The variation of the gradient cannot be explained in a similar manner. The variation observed for V1504 Cyg is different from that observed for KIC 8751494, which might point towards a difference in accretion disc between these two objects. This is possibly due to the fact that V1504 Cyg is a SU UMa dwarf nova and KIC 8751494 a nova-like variable. However, further research is needed.

When sampling a single time scale, the gradient and intercept of the fitted rms-flux relation also vary with the quiescent data set under consideration. As different data sets are observed at different times, the parameters of the fitted rms-flux relation vary with time. For KIC 8751494, only four quiescent data sets are available. In order to determine any variation, more data is needed. For V1504 Cyg, there is a clear variation of gradient with time, but only over a period of approximately a year. Before and after this period, the measured gradients appear scattered. The intercept appears to decrease with time, but the data is again scattered. Further research is needed in order to quantify any present variations of gradient and intercept with time and determine their origin.

The rms-flux relation implies that short and long flickering time scales are coupled together. This is reproduced by the fluctuating accretion model. In this model, flickering variability originates throughout the accretion disc and modulates the central emission. The different time scales at which flickering variability occur are coupled together multiplicatively, hence coupling short and long time scales and producing the rms-flux relation. The multiplicative coupling of time scales also produces a lognormal flux distribution, another property of flickering variability. When different time scales are added together instead of multiplied, as is done in the shot noise model, the short and long time scales are not coupled. The shot noise model hence does not replicate the rms-flux relation and the lognormal flux distribution.

We have briefly analysed the flux distribution of V1504 Cyg and KIC 8751494. The distributions of all quiescent data sets appear to be lognormal. However, a lognormal model needs to be fit to these distributions in order to obtain a goodness-of-fit.

The detection of the rms-flux relation in V1504 Cyg and KIC 8751494, together with its detection in MV Lyr, brings the total number of CVs with a detected rms-flux relation to three. This enforces the hypothesis of the universal nature of accretion-induced variability. It is very likely that the rms-flux relation will be observed in the other six CVs when data of sufficient quality will be available for these systems.

Bibliography

[1] H.J. Adèr and G.J. Mellenbergh. *Advising on Research Methods: A Consultant's Companion*. Johannes Van Kessel Publishing, 2008.

[2] Sangtae Ahn and Jeffrey A Fessler. Standard errors of mean, variance, and standard deviation estimators. *University of Michigan: EECS Department*, 2003.

[3] R. Andrae, T. Schulze-Hartung, and P. Melchior. Dos and don'ts of reduced chi-squared. *ArXiv e-prints*, December 2010.

[4] P. Arevalo and P. Uttley. Investigating a fluctuating-accretion model for the spectral-timing properties of accreting black hole systems. *Monthly Notices of the Royal Astronomical Society*, 367(2):801–814, April 2006.

[5] T. Belloni and G. Hasinger. An atlas of aperiodic variability in HMXB. *Astronomy and Astrophysics*, 230:103–119, April 1990.

[6] T. Belloni, D. Psaltis, and M. van der Klis. A Unified Description of the Timing Features of Accreting X-Ray Binaries. *Astrophysical Journal*, 572:392–406, June 2002.

[7] A. Bruch. Long-term photometry of the eclipsing dwarf nova V893 Scorpii: Orbital period, oscillations, and a possible giant planet. *ArXiv e-prints*, April 2014.

[8] P. Cassatella, P. Uttley, J. Wilms, and J. Poutanen. Joint spectral-timing modelling of the hard lags in GX 339-4: constraints on reflection models. *Monthly Notices of the Royal Astronomical Society*, 422:2407–2416, May 2012.

[9] Ronald A. Downes, Ronald F. Webbink, Michael M. Shara, Hans Ritter, Ulrich Kolb, and Hilmar W. Duerbeck. A Catalog and Atlas of Cataclysmic Variables: The Living Edition. *Publications of the Astronomical Society of the Pacific*, 113(784):764–768, June 2001.

[10] B. Efron. Bootstrap Methods: Another Look at the Jackknife. *The Annals of Statistics*, 7(1):1–26, January 1979.

[11] J. J. Feldmeier, S. B. Howell, W. Sherry, K. von Braun, M. E. Everett, D. R. Ciardi, P. Harding, J. C. Mihos, C. S. Rudick, T.-H. Lee, R. M. Kutsko, and G. T. van Belle. The Burrell-Optical-Kepler-Survey (BOKS). I. Survey Description and Initial Results. *The Astronomical Journal*, 142:2, July 2011.

[12] J. Frank, A. King, and D. J. Raine. *Accretion Power in Astrophysics: Third Edition*. Cambridge University Press, January 2002.

[13] J. Frank, A. R. King, and D. J. Raine. *Accretion power in astrophysics*. Cambridge University Press, 1985.

[14] Revision 4: Dorothy Fraquelli and Susan E. Thompson. Kepler Archive Manual (KDMC-10008-004). Technical report, Space Telescope Science Institute, April 2012.

[15] P. Gandhi. The Flux-Dependent rms Variability of X-Ray Binaries in the Optical. *The Astrophysical Journal Letters*, 697:L167–L172, June 2009.

[16] R. L. Gilliland, W. J. Chaplin, E. W. Dunham, V. S. Argabright, W. J. Borucki, G. Basri, S. T. Bryson, D. L. Buzasi, D. A. Caldwell, Y. P. Elsworth, J. M. Jenkins, D. G. Koch, J. Kolodziejczak, A. Miglio, J. van Cleve, L. M. Walkowicz, and W. F. Welsh. Kepler Mission Stellar and Instrument Noise Properties. *The Astrophysical Journal Supplement*, 197:6, November 2011.

[17] R. L. Gilliland, J. M. Jenkins, W. J. Borucki, S. T. Bryson, D. A. Caldwell, B. D. Clarke, J. L. Dotson, M. R. Haas, J. Hall, T. Klaus, D. Koch, S. McCauliff, E. V. Quintana, J. D. Twicken, and J. E. van Cleve. Initial Characteristics of Kepler Short Cadence Data. *The Astrophysical Journal Letters*, 713:L160–L163, April 2010.

[18] M. R. Haas, N. M. Batalha, S. T. Bryson, D. A. Caldwell, J. L. Dotson, J. Hall, J. M. Jenkins, T. C. Klaus, D. G. Koch, J. Kolodziejczak, C. Middour, M. Smith, C. K. Sobeck, J. Stober, R. S. Thompson, and J. E. Van Cleve. Kepler Science Operations. *The Astrophysical Journal Letters*, 713:L115–L119, April 2010.

[19] C. Hellier. *Cataclysmic Variable Stars - How and Why they Vary*. Springer, January 2001.

[20] S. B. Howell, C. Sobeck, M. Haas, M. Still, T. Barclay, F. Mullally, J. Troeltzsch, S. Aigrain, S. T. Bryson, D. Caldwell, W. J. Chaplin, W. D. Cochran, D. Huber, G. W. Marcy, A. Miglio, J. R. Najita, M. Smith, J. D. Twicken, and J. J. Fortney. The K2 Mission: Characterization and Early results. *ArXiv e-prints*, February 2014.

[21] Steve B. Howell, Mark E. Everett, Sally A. Seebode, Paula Szkody, Martin Still, Matt Wood, Gavin Ramsay, John Cannizzo, and Alan Smale. Spectroscopy of new and poorly known cataclysmic variables in the Kepler field. *The Astronomical Journal*, 145(4):109, April 2013.

[22] Enthought Inc. The Enthought Python Distribution, version 7.3. http://www.enthought.com/epd, 2008–. Last visited on 17/1/2014.

[23] A. Ingram and M. van der Klis. An exact analytic treatment of propagating mass accretion rate fluctuations in X-ray binaries. *Monthly Notices of the Royal Astronomical Society*, 434:1476–1485, September 2013.

[24] KU Leuven Instituut voor Sterrenkunde. IvS Python repository. http://www.ster.kuleuven.be/~pieterd/python/html/ivs/ivs_index.html. Last visited on 20/10/2013.

[25] J. M. Jenkins, D. A. Caldwell, H. Chandrasekaran, J. D. Twicken, S. T. Bryson, E. V. Quintana, B. D. Clarke, J. Li, C. Allen, P. Tenenbaum, H. Wu, T. C. Klaus, C. K. Middour, M. T. Cote, S. McCauliff, F. R. Girouard, J. P. Gunter, B. Wohler, J. Sommers, J. R. Hall, A. K. Uddin, M. S. Wu, P. A. Bhavsar, J. Van Cleve, D. L. Pletcher, J. A. Dotson, M. R. Haas, R. L. Gilliland, D. G. Koch, and W. J. Borucki. Overview of the Kepler Science Processing Pipeline. *The Astrophysical Journal Letters*, 713:L87–L91, April 2010.

[26] Eric Jones, Travis Oliphant, Pearu Peterson, et al. SciPy: Open source scientific tools for Python. http://www.scipy.org/, 2001–. Last visited on 3/6/2014.

[27] T. Kato and H. Maehara. Analysis of a Kepler Light Curve of the Novalike Cataclysmic Variable KIC 8751494. *Publications of the Astronomical Society of Japan*, 65:76, August 2013.

[28] T. Kato and Y. Osaki. Analysis of Three SU UMa-Type Dwarf Novae in the Kepler Field. *Publications of the Astronomical Society of Japan*, 65:97, October 2013.

[29] Taichi Kato. Discovery of a new SU UMa-type dwarf nova V344 Lyrae. *Publications of the Astronomical Society of Japan*, 45, 1993.

[30] C. Knigge. The Evolution of Cataclysmic Variables. In L. Schmidtobreick, M. R. Schreiber, and C. Tappert, editors, *Evolution of Compact Binaries*, volume 447 of *Astronomical Society of the Pacific Conference Series*, page 3, September 2011.

[31] C. Knigge, I. Baraffe, and J. Patterson. The Evolution of Cataclysmic Variables as Revealed by Their Donor Stars. *The Astrophysical Journal Supplement*, 194:28, June 2011.

[32] O. Kotov, E. Churazov, and M. Gilfanov. On the X-ray time-lags in the black hole candidates. *Monthly Notices of the Royal Astronomical Society*, 327:799–807, November 2001.

[33] Y. E. Lyubarskii. Flicker noise in accretion discs. *Monthly Notices of the Royal Astronomical Society*, 292:679, December 1997.

[34] S. Miyamoto, K. Kimura, S. Kitamoto, T. Dotani, and K. Ebisawa. X-ray variability of GX 339 - 4 in its very high state. *Astrophysical Journal*, 383:784–807, December 1991.

[35] D. Nogami and S. Masuda. Confirmation of the SU UMa nature of V1504 Cyg. *Information Bulletin on Variable Stars*, 1997.

[36] G. Ramsay, S. B. Howell, M. A. Wood, A. Smale, T. Barclay, S. A. Seebode, D. Gelino, M. Still, and J. K. Cannizzo. BOKS 45906: a CV with an orbital period of 56.6 min in the Kepler field? *Monthly Notices of the Royal Astronomical Society*, 438:789–795, February 2014.

[37] Gavin Ramsay, John K. Cannizzo, Steve B. Howell, Matt A. Wood, Martin Still, Thomas Barclay, and Alan Smale. Kepler observations of V447 Lyr: an eclipsing U Gem Cataclysmic Variable. *Monthly Notices of the Royal Astronomical Society*, 425(2):1479–1485, September 2012.

[38] N. N. Samus, O. V. Durlevich, and et al. General Catalogue of Variable Stars (Samus+ 2007-2013). *VizieR Online Data Catalog*, 1:2025, January 2009.

[39] S. Scaringi. A physical model for the flickering variability in cataclysmic variables. *Monthly Notices of the Royal Astronomical Society*, 438:1233–1241, February 2014.

[40] S. Scaringi, P. J. Groot, K. Verbeek, S. Greiss, C. Knigge, and E. Körding. Spectroscopic identifications of blue-Hα-excess sources in the Kepler field of view. *Monthly Notices of the Royal Astronomical Society*, 428:2207–2215, January 2013.

[41] S. Scaringi, E. Körding, P. J. Groot, P. Uttley, T. Marsh, C. Knigge, T. Maccarone, and V. S. Dhillon. Discovery of Fourier-dependent time lags in cataclysmic variables. *Monthly Notices of the Royal Astronomical Society*, 431:2535–2541, May 2013.

[42] S. Scaringi, E. Körding, P. Uttley, P. J. Groot, C. Knigge, M. Still, and P. Jonker. Broad-band timing properties of the accreting white dwarf MV Lyrae. *Monthly Notices of the Royal Astronomical Society*, 427(4):3396–3405, January 2013.

[43] S. Scaringi, E. Körding, P. Uttley, C. Knigge, P. J. Groot, and M. Still. The Universal Nature of Accretion-induced Variability: The RMS-Flux Relation in an Accreting White Dwarf. *Monthly Notices of the Royal Astronomical Society*, page 7, January 2012.

[44] N. I. Shakura and R. A. Sunyaev. Black holes in binary systems. Observational appearance. *Astronomy and Astrophysics*, 24:337–355, 1973.

[45] M. Still, S. B. Howell, M. A. Wood, J. K. Cannizzo, and A. P. Smale. Quiescent Superhumps Detected in the Dwarf Nova V344 Lyrae by Kepler. *The Astrophysical Journal Letters*, 717:L113–L117, July 2010.

[46] Martin Still. K2 - extending kepler's power to the ecliptic. http://keplerscience.arc.nasa.gov/K2/. Last visited on 5/6/2014.

[47] J. Timmer and M. Koenig. On generating power law noise. *Astronomy and Astrophysics*, 300:707, August 1995.

[48] P. Uttley and I. M. McHardy. The flux-dependent amplitude of broadband noise variability in X-ray binaries and active galaxies. *Monthly Notices of the Royal Astronomical Society*, 323(2):L26–L30, May 2001.

[49] P. Uttley, I. M. McHardy, and S. Vaughan. Non-linear X-ray variability in X-ray binaries and active galaxies. *Monthly Notices of the Royal Astronomical Society*, 359(1):345–362, May 2005.

[50] Brian A. Vaughan and Michael A. Nowak. X-Ray Variability Coherence: How to Compute It, What It Means, and How It Constrains Models of GX 3394 and Cygnus X-1. *The Astrophysical Journal*, 474(1):L43–L46, January 1997.

[51] S. Vaughan, R. Edelson, R. S. Warwick, and P. Uttley. On characterizing the variability properties of X-ray light curves from active galaxies. *Monthly Notices of the Royal Astronomical Society*, 345:1271–1284, November 2003.

[52] F. Verbunt. Accretion disks in stellar X-ray sources - A review of the basic theory of accretion disks and its problems. *Space Science Reviews*, 32:379–404, 1982.

[53] B. Warner. Rapid Oscillations in Cataclysmic Variables. *The Publications of the Astronomical Society of the Pacific*, 116:115–132, February 2004.

[54] B. Warner, P. A. Woudt, and M. L. Pretorius. Dwarf nova oscillations and quasi-periodic oscillations in cataclysmic variables - III. A new kind of dwarf nova oscillation, and further examples of the similarities to X-ray binaries. *Monthly Notices of the Royal Astronomical Society*, 344:1193–1209, October 2003.

[55] Brian Warner. *Cataclysmic Variable Stars*. Cambridge University Press, 2003.

[56] Eric W. Weisstein. Spearman rank correlation coefficient. From MathWorld — A Wolfram Web Resource. http://mathworld.wolfram.com/SpearmanRankCorrelationCoefficient.html. Last visited on 26/5/2014.

[57] Kurtis A. Williams, Domitilla de Martino, Roberto Silvotti, Ivan Bruni, Patrick Dufour, Thomas S. Riecken, Martin Kronberg, Anjum Mukadam, and G. Handler. Discovery of a nova-like cataclysmic variable in the Kepler mission field. *The Astronomical Journal*, 139(6):2587–2594, June 2010.

[58] M.A. Wood, M. D. Still, S. B. Howell, J. K. Cannizzo, and A. P. Smale. V344 Lyrae: A Touchstone SU UMa Cataclysmic Variable in the Kepler Field. *The Astrophysical Journal*, 741:105, November 2011.

[59] Matthew A. Wood, M.D. Still, S.B. Howell, J.K. Cannizzo, A.P. Smale, G. Ramsay, and T. Barclay. 2.5 Years of Kepler Short Cadence Observations of the Cataclysmic Variable V1504 Cyg. *American Astronomical Society*, 2013.

Appendix A

Period determination

Peaks are clearly visible in some of the PSDs shown in figures 5.5 and 5.6. These peaks may correspond to the periods characteristic to the system, such as the orbital and superhump period, and their harmonics. In this appendix, we investigate all PSDs of all quiescent data sets of the CVs listed in 3.1, and determine the periods corresponding to any clearly visible peaks. We then compare the periods found to those listed in literature. The periods found in literature are given in table A.1.

In section A.1, we will expand on the data analysis method used to find the periods corresponding to the peaks. In section A.2, the periods found will be discussed and compared to those found in literature.

Object	P_{orb}	$P_{SH,+}$	$P_{SH,-}$	Source
BOKS 45906	56.5574 ± 0.0014 min			[36]
V344 Lyr	2.11 h	2.20 h	2.06 h	[58]
V363 Lyr	4.68 h	4.47 h		[36]
V447 Lyr	3.74 h			[37]
V516 Lyr	2.0159952 ± 0.000005 h			[28]
V1504 Cyg	1.66971 ± 0.00002 h	1.74 h	1.63 h	[59]
KIC 8751494	2.7451008 ± 0.0000002 h	2.9388 h		[27]

Table A.1: Orbital period P_{orb}, positive superhump period $P_{SH,+}$, and negative superhump period $P_{SH,-}$ found in literature for the CVs listed in table 3.1. No periods were found for V452 Lyr and V585 Lyr.

A.1 Data analysis method

The programming language Python is used to perform the data analysis. For every object, we first calculate the PSD for every data set available. Whenever a peak is clearly visible in a PSD, we plot the *periodogram* of that data set. A periodogram is calculated in the same way as the PSD, but it is plotted on a linear scale instead of a logarithmic scale. The different scale makes it easier to detect the peak, which will be illustrated in the following section.

The location of the peak is determined by searching for the frequency with the most power in a certain frequency range, and the frequency corresponding to it is found accordingly. In order to determine the error on the frequency, the data is bootstrapped. The frequency is then converted to a period, as this is more conventional in CVs. The error is converted via error propagation. This is done via

$$P = \frac{f}{3600},\ \delta P = P\frac{\delta f}{f} = \frac{\delta f}{3600 f^2}, \tag{A.1}$$

with P the period in hours, f the frequency in Hz, and δP and δf their respective errors.

A.2 Results

We will now discuss the results of the data analysis of all CVs. As expected, no periods were visible in V585 Lyr. For V363 Lyr and V516 Lyr, periods are listed in literature, but we could not detect them in their respective quiescent intervals. Their characteristic periods most likely have not been detected as we only considered the quiescent intervals in the data analysis [28, 36]. The detection of the periods of the other five CVs will be discussed in the following sections.

A.2.1 BOKS 45906

Figure A.1 shows the PSD and periodogram of the combined quiescent intervals of Q7 of BOKS 45906. A peak is clearly visible in both. This peak is visible in all data sets and corresponds to the orbital period of the system. After analysing all data sets, we find that $P_{orb} = 0.94 \pm 0.03$ h. This period corresponds to the orbital period found in literature [36].

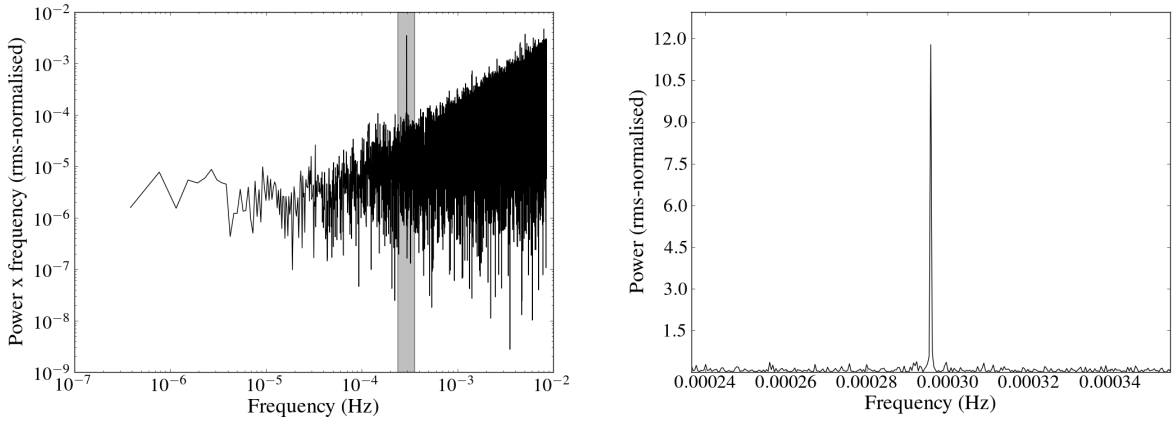

(a) Rms-normalised PSD (b) Periodogram

Figure A.1: The rms-normalised PSD and periodogram of the combined quiescent intervals of Q7 of BOKS 45906 are shown. The peak in the PSD under investigation is marked by the shaded region. This region marks the range over which the periodogram is plotted.

A.2.2 V344 Lyr

The PSD and periodogram of the combined quiescent intervals of Q2 of V344 Lyr are shown in figure A.2. The highest peak is not as narrow as the peak found in the data sets of BOKS 45906. This is because the orbital period, positive superhump period and negative superhump period do not differ that much, giving rise to a broadened peak. Harmonics of the orbital period are also clearly visible.

Not all data sets of V344 Lyr show visible peaks. The orbital period could be detected, but the period and its error depend on the data set analysed. The most conservative period is 2.12 ± 0.05 h, which corresponds to the period found in literature. The positive and negative superhump period have been detected in some data sets. We find a positive superhump period of 2.19 ± 0.08 h and a negative superhump period of 2.06 ± 0.02 h. These values also in correspond to the periods found in literature [58]. The period causing the peak with the highest power varies over all data sets. This is because the relative power the orbital period, positive and negative superhump period varies with time [45].

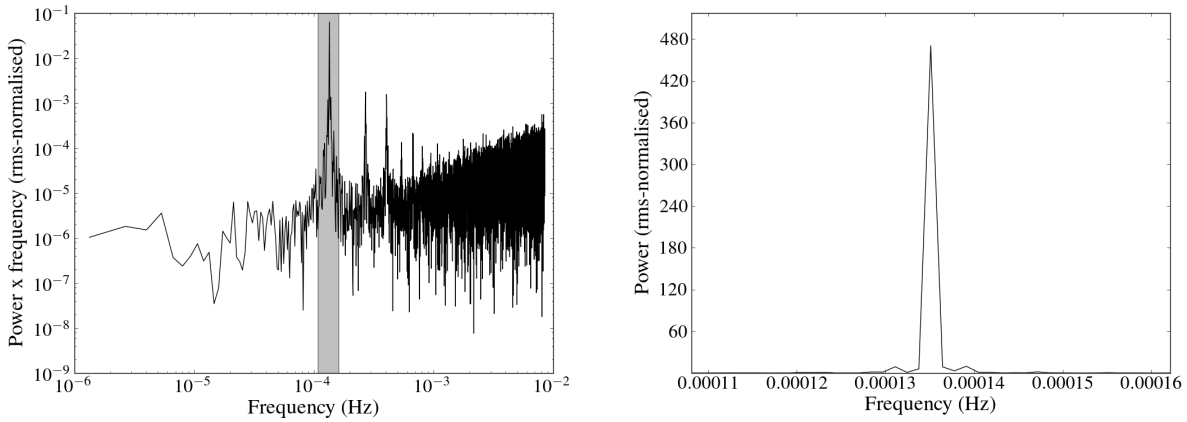

(a) Rms-normalised PSD (b) Periodogram

Figure A.2: The rms-normalised PSD and periodogram of the combined quiescent intervals of Q2 of V344 Lyr are shown. TThe peak in the PSD under investigation is marked by the shaded region. This region marks the range over which the periodogram is plotted.

A.2.3 V447 Lyr

In figure A.3, the PSD and periodogram of one of the quiescent intervals of V447 Lyr are shown. A peak and its harmonics are clearly visible in the PSD, and are caused by the orbital period of the system. These peaks are visible in all data sets. However, the period and its error determined by the data analysis depends on the data set analysed. The most conservative period found is 3.72 ± 0.03 h. This period corresponds to the period found in literature [37].

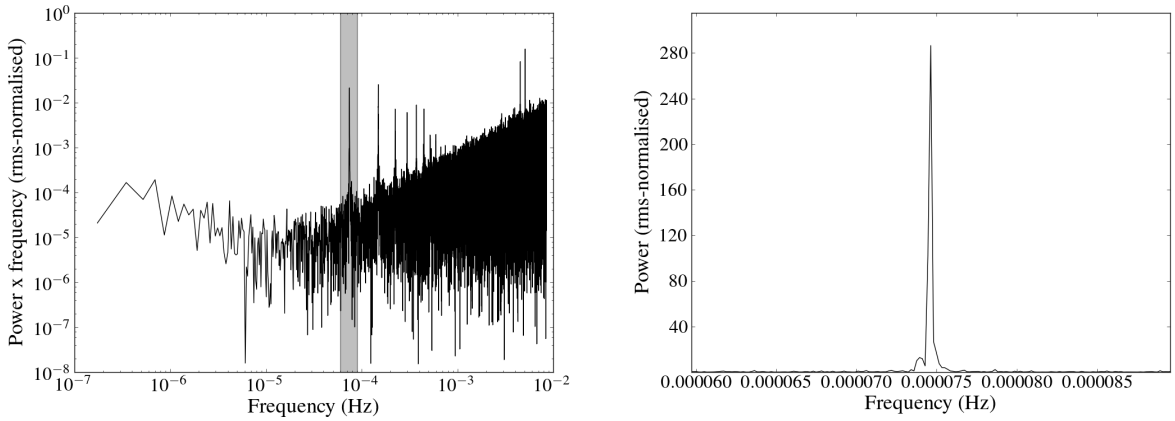

(a) Rms-normalised PSD (b) Periodogram

Figure A.3: The rms-normalised PSD and periodogram of the combined quiescent intervals of Q15 in V447 Lyr are shown. The peak in the PSD under investigation is marked by the shaded region. This region marks the range over which the periodogram is plotted.

A.2.4 V1504 Cyg

In figure A.4 the PSD and periodogram of the combined quiescent intervals of Q15 of V1504 Cyg. In this data set, the orbital period of the system is clearly visible. The negative superhump period is also visible in the periodogram.

Not all data sets of V1504 Cyg show visible peaks. The orbital period could be detected, but the period and its error depend on the data set analysed. The most conservative period found is 1.66 ± 0.03 h. The positive superhump period was visible in few data sets, in each of these data sets we found a period of 1.72 ± 0.03 h. The negative superhump period was also visible in few data sets, the most conservative period found is 1.63 ± 0.03 h. All periods found correspond to those found in literature [59].

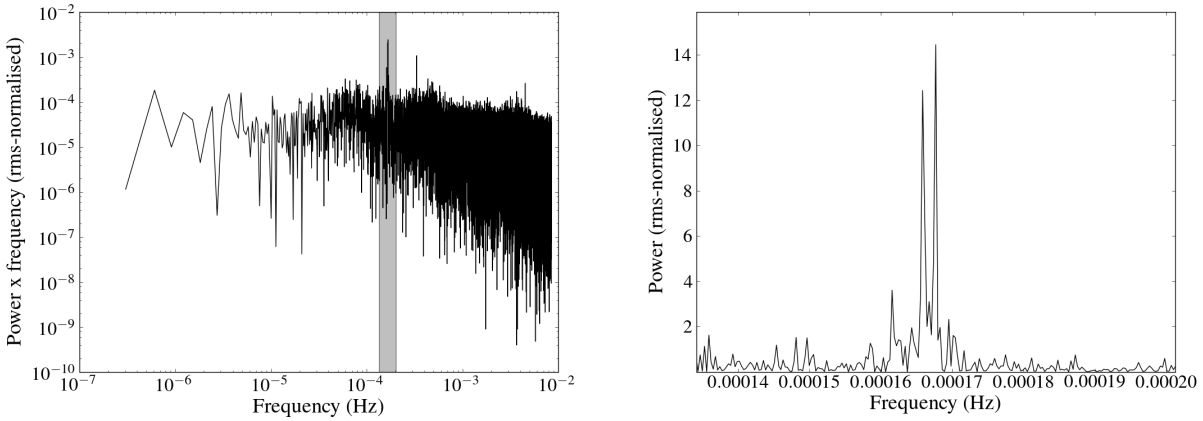

(a) Rms-normalised PSD (b) Periodogram

Figure A.4: The rms-normalised PSD and periodogram of the combined quiescent intervals of Q15 of V1504 Cyg are shown. The peak in the PSD under investigation is marked by the shaded region. This region marks the range over which the periodogram is plotted.

A.2.5 KIC 8751494

Figure A.5 shows the PSD and periodogram of the combined quiescent intervals of Q2 of KIC 8751494. A peak is clearly visible in both, and is caused by the positive superhump period. We find that this peak corresponds to 2.93 ± 0.03 h, which corresponds to the positive superhump period found in literature [27]. The orbital period of the system was not found.

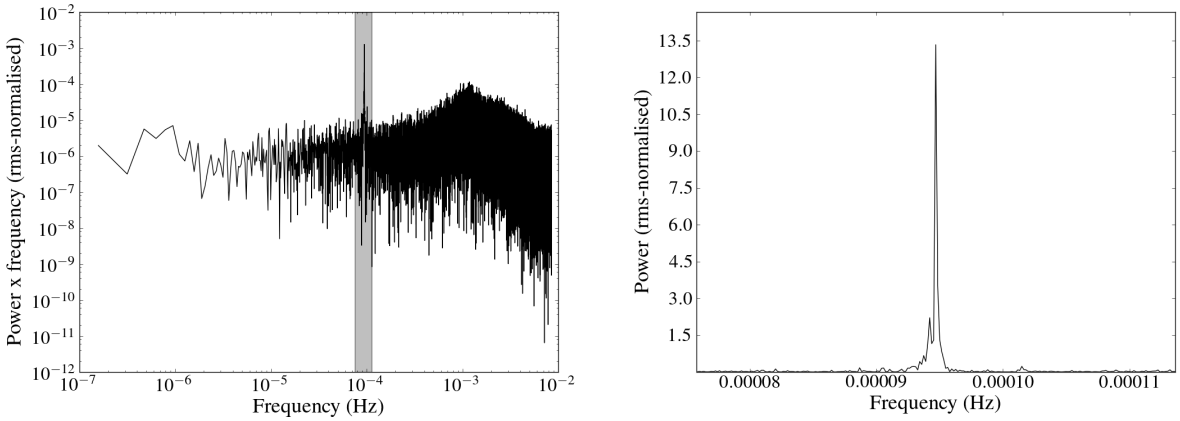

(a) Rms-normalised PSD

(b) Periodogram

Figure A.5: The rms-normalised PSD and periodogram of the combined quiescent intervals of Q16 of KIC 8751494 are shown. The peak in the PSD under investigation is marked by the shaded region. This region marks the range over which the periodogram is plotted.

INSTITUUT VOOR STERRENKUNDE
Celestijnenlaan 200D bus 2401
3001 HEVERLEE, BELGIË
tel. + 32 16 32 70 27
fax + 32 16 32 79 99
www.kuleuven.be